COMPARING HYDROCARBON VOLUME BETWEEN LSA (LAMINATED SAND ANALYSIS) AND STANDARD TECHNIQUES IN LOW RESISTIVITY SANDSTONE RESERVOIRS

BY

Omar Abdullah Ba-Wazir

A Thesis Presented to the

DEANSHIP OF GRADUATE STUDIES

KING FAHD UNIVERSITY OF PETROLEUM & MINERALS

DHAHRAN, SAUDI ARABIA

In Partial Fulfillment of the
Requirements for the Degree of

MASTER OF SCIENCE

In

GEOLOGY

April, 2013

KING FAHD UNIVERSITY OF PETROLEUM & MINERALS

DHAHRAN- 31261, SAUDI ARABIA

DEANSHIP OF GRADUATE STUDIES

This thesis, written by **Omar Abdullah Ba-Wazir** under the direction his thesis advisor and approved by his thesis committee, has been presented and accepted by the Dean of Graduate Studies, in partial fulfillment of the requirements for the degree of **MASTER OF SCIENCE IN GEOLOGY.**

Dr. Gabor Korvin
(Advisor)

Dr. Abdulazeez Al-Shaibani
Department Chairman

Dr. Osman Abdullatif
(Member)

Dr. Salam A. Zummo
Dean of Graduate Studies

Dr. Abdulazeez Abdulraheem
(Member)

19/5/13
Date

I would like to dedicate my thesis to my family, starting from my parents and then my sisters for their patient and support, and special dedication for my young brother Saeed to continue his study to the highest levels.

ACKNOWLEDGMENTS

I would like first to thank King Fahd University of Petroleum and Minerals for giving me the opportunity to achieve Master Degree in Geology after completing Bachelor Degree in Geophysics in the Earth Science Department.

I'm grateful to Schlumberger for providing, supporting and guiding the results and for the fruitful discussions with the technical experts in Schlumberger with full accessible to the software.

Special thanks to the Professor Dr. Gabor Korvin for his advices, assistance and sharing his expertise in Petrophysical measurements and Well logging.

TABLE OF CONTENTS

LIST OF TABLES

LIST OF FIGURES

LIST OF ABBREVIATIONS

LRP	:	Low Resistivity Pay
LRLC	:	Low Resistivity Low Contrast
HRLC	:	High Resistivity Low Contrast pay
R_v	:	Vertical resistivity
R_h	:	Horizontal resistivity
NMR	:	Nuclear Magnetic Resonance
Rsand	:	Sand Resistivity
LSA	:	Laminated Sand Analysis
σ_t	:	Total conductivity measurement
Vshale	:	Volume fraction of shale
Vsand	:	volume fraction of sand
$\boldsymbol{\sigma_{shale}}$	:	Conductivity measurement of Shale
σ_{sand}	:	Conductivity measurement of Sand
R_{shh}	:	Horizontal Shale Resistivity
R_{shv}	:	Vertical Shale Resistivity
F_{sand}	:	Volume fraction of sand

Fsh_Lam	:	Volume fraction of laminated shale in sand fraction
$\emptyset_{dis\_clay}$	:	Clay water fraction in the dispersed clay
V_{xbw}	:	Total clay bound water
R_{sd}	:	Gamma ray counting rate of the sand fraction
Y_{sd}	:	Counting yield of the sand
A_{sd}	:	Sand activity
R_{sh}	:	Gamma ray counting rate of the shale fraction
Y_{sh}	:	Counting yield of the shale
A_{sh}	:	Shale activity
$\emptyset_{sd}$	:	Clean Sand porosity
$\emptyset_{sh}$	:	Shale porosity
$\emptyset_{dis\_sd}$	:	Dispersed Sand Porosity
$X_{sh,dis}$	:	Shale fraction in the sand pore space
$X_{sh,lam}$	:	Shale fraction in the lamination
X_{sd}	:	Sand fraction in the lamination.

ABSTRACT

Full Name : [Omar Abdullah Saeed Ba-Wazir]

Thesis Title : [COMPARING HYDROCARBON VOLUME BETWEEN LSA (LAMINATED SAND ANALYSIS) AND STANDARD TECHNIQUES IN LOW RESISTIVITY SANDSTONE RESERVOIRS]

Major Field : [Geology]

Date of Degree : [April 2013]

Thinly laminated formations, composed of sand-shale sequences, refer to beds of thickness that are below the vertical resolution of standard formation evaluation log measurements. These thinly bedded formations could be significant hydrocarbon reservoirs particularly in turbidite or fluvial depositional environments, which are usually showing mixture of fine and coarse grains.

Standard formation evaluation methods using conventional logs (Gamma ray-formation resistivity-Neutron and Density) in the thinly bedded formations overestimate the volume of clay (VCL) and underestimate porosity and hydrocarbon saturations.

Advanced analyses are required to fully characterize and evaluate the property of thin beds and to obtain improved hydrocarbon estimations. Such analyses are provided by the Laminated Sand Analysis (LSA) techniques that use data including Wireline Nuclear Magnetic Resonance (NMR), Resistivity Borehole Images and Triaxial resistivity logs.

In the Thesis I worked out two case studies, in fluvial and turbidite environments, in order to better evaluate thinly bedded intervals within clastic reservoirs. I applied LSA

techniques in these two case studies in which the formation evaluation was computed and compared with the standard formation evaluation using conventional logs.

ملخص الرسالة

الاسم الكامل:عمر عبدالله سعيد باوزير

عنوان الرسالة: مقارنة الناتج الهيدروكربوني من خزانات الحجر الرملي, ذات المقاومة الكهربائية المنخفضة , بين الطرق الأعتيادية للتحليل والطرق الحديثة المتعلقة بتحليل الحجر الرملي الهيدروكربوني بين طبقات معادن الطفل.

التخصص: جيولوجيا

تاريخ الدرجة العلمية:أبريل (نيسان)2013

الطبقات التسلسلية المكونة من الحجر الرملي و معادن الطفل هي طبقات ذات سماكة رقيقة بحيث يصعب كشف كل طبقة بالطرق الاعتيادية للتحليل.

تكمن أهمية هذه الطبقات في الرواسب المتكونة بأعماق المحيط أو المتكونة في البيئات النهرية التي عادة ما تشكل أهمية لخزانات النفط والغاز بين مكونات تلك الطبقات.

الطرق الاعتيادية للتحليل باستخدام أشعات جاما, المقاومة الكهربائية الأفقية, و قياس كميات النيوترونات و الكثافة لتحديد طبقات الحجر الرملي ذات المتكون الهيدروكربوني , تسهم بشكل عام في تضخيم حجم معادن الطفل بين تلك الطبقات وبالتالي تقليل مسامية الحجر الرملي الزيتي.

هناك حاجة الى تحليلات متقدمة لاعطاء وصف كامل و تقييم طبقات الحجر الرملي ذات المتكون الهيدروكربوني. هذه التحليلات تشمل الرنين النووي المغناطيسي, الصور المقطعية للأبار و سجلات المقاومة الكهربائية ثلاثية المحاور.

في هذه الرسالة, قدمت نموذجين مختلفين لتوضيح أهمية هذه التحليلات المتقدمة مقارنة بالطرق الاعتيادية لتحليل طبقات الحجر الرملي الزيتي بين معادن الطفل. النموذج الأول من بيئة نهرية و النموذج الثاني مقتبس من أحد المكامن داخل أعماق المحيط.

CHAPTER 1

INTRODUCTION

1.1 Introduction

The concept “Low Contrast Pay (LCP)” is defined as the pay exhibiting low contrast in distinguishing between hydrocarbon and water bearing zones from borehole logs. This contrast between hydrocarbon and water zones is best described by resistivity measurements to compute accurate fluid saturations. Therefore, Low Contrast Pays can be classified as low Resistivity Low Contrast Pays (LRLC) or High Resistivity Low Contrast Pays (HRLC), depending on the range of the resistivity values measured. In HRLC reservoirs everything appears hydrocarbon-bearing, while LRLC reservoirs are often difficult to recognize and can easily be overlooked, since everything appears to be wet (Shahid, M.. et al. 2008). In the LRLC reservoirs, the resistivity data interpretations indicate high water saturation, while actually oil or even dry oil will be produced.

LRLC pays are found worldwide in complex reservoirs, but it is worth noting that the hydrocarbon volumes present in large fractions of overbank deposits composed of thin-bed laminations of sand and shale layers are characterized as low resistivity low contrast pays (LRLC). Therefore the thin-bedded low resistivity pay regions cause the resistivity of thin sands, which may contain hydrocarbon, to be reduced by the bound water in the

clay laminations as well as the high conductivity of the silt. As a result, the true petrophysical properties (porosity, permeability and saturation) will be underestimated. Many techniques have been discovered later to help log analyst to more properly interpret the hydrocarbon-bearing thin-bedded low resistivity pay regions.

This Thesis focuses on the advantages of combining all these recent techniques that are called "Laminated Sand Analysis (LSA)" techniques and to make a comparison between them in laminated shaly-sand reservoirs. These LSA techniques include Triaxial Resistivity Induction logs (Multicomponent Induction Resistivity logs), Nuclear Magnetic Resonance (NMR) and High-Resolution Borehole Image. I will discuss two examples of thinly bedded shaly-sand reservoirs in order to show the improvement in hydrocarbon volumes and the accuracy of fluid saturation in comparison with the traditional analysis that depends only on the conventional logs (Gamma ray-Neutron-Density and Resistivity).

1.2 Problem Statement

A formation composed of thin layers of small pore size rocks (shale) and coarser high permeability rocks (sand) gives a very misleading resistivity response from which it is difficult to determine whether the formation will flow hydrocarbon or water. Determination of accurate sand volume in such thinly bedded sand-shale formation by only conventional logs (Gamma Ray, Deep Resistivity Log, and Neutron-Density) could be at their limits and might not be conclusive, particularly in exploration wells, where no core data are available yet. Therefore, the challenge is how to best quantify hydrocarbon in place from these available open hole logs.

1.3 Objectives

I work out and discuss two case studies of different locations in the Thesis. Both relate to thin-bedded clastic formations that are exhibiting low resistivity values.

I will make formation evaluations using two techniques and show comparison them. These techniques are conventional analysis, using only Gamma Ray, Deep resistivity log, and Neutron-Density, and Laminated Sand Analysis LSA, using interpretations from the following analyses:

- Wireline Nuclear Magnetic Resonance (NMR) to detect Low Resistivity Pays by separating free fluid and bound fluid volumes,
- High Resolution Borehole Images to show clear evidences of lamination and invert for the true (high resolution) log response for each bed or layer.
- Triaxial Resistivity Induction logs to derive both Horizontal resistivity Rh (resistivity that is parallel to the bedding) and Vertical Resistivity Rv (resistivity that is perpendicular to the bedding) and invert the true sand resistivity Rsand in the laminations.

1.4 Methodology

I generally applied the following workflow based on the data availability. Additional specific analyses will be highlighted in each case separately.

1) Gather the available open hole logs from the two case studies separately.
2) Apply environmental correction and depth-matching between logs.
3) Compute the formation evaluation using simple shaly-sand model from the conventional logs (Gamma Ray, Deep Resistivity Log, and Neutron-Density).
4) Process the NMR logs.
5) Process the borehole image logs and compute the high resolution resistivity curve (SRES) from one pad of the image.
6) The standard resolution logs are depth-matched to SRES curve.
7) Process Triaxial Resistivity Induction logs using 1D-inversion algorithm to generate Rv and Rh.
8) Recompute the formation evaluation using the processed techniques from steps (4,5,6,7) in addition to the conventional logs.
9) Compare the two formation evaluation results in the thin bed zones.

CHAPTER 2

Geological Setting

Thin bed formations occur in any sand/siltstone that has undergone digenesis, as in turbidite (deep water) and fluvial environments (Clavaud, J., et at. 2005).

2.1 Deep Water (Turbidite) Environments

Turbiditic environment is defined as a basin fill in water depths greater than 500 m . They are clastic sediments transported beyond the shelf edge into deep water by sediment gravity flow and deposited on the continental slope and in the basin. They are later buried and become part of a basin fill, as shown in Figure 1(Slatt, R., 2001, and Weimer, P., and Slatt, R. 2004).

Thin beds form in deep water settings as levee-overbank, channel margin and sheet sands, as shown in Figure 2.

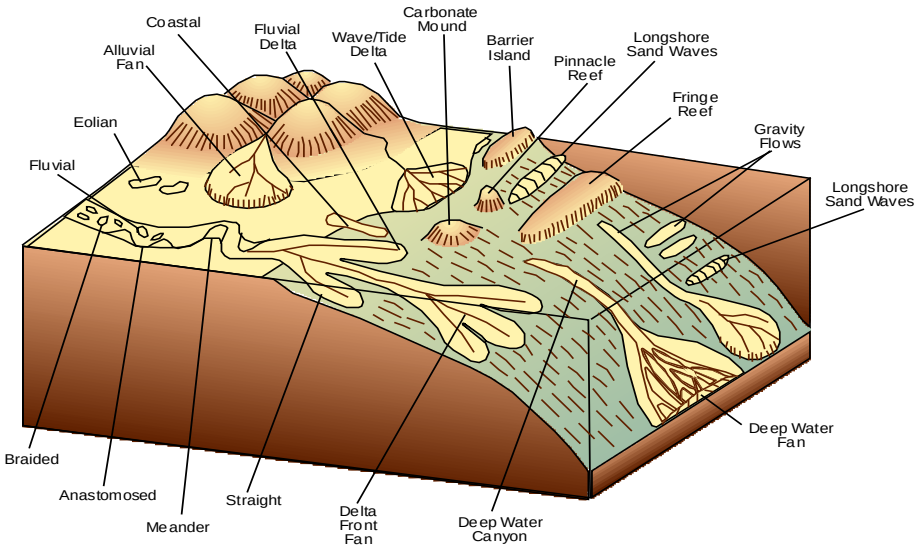

Figure 1.LRP (Thin-bed zones) can potentially be found in fluvial and turbidite environments (Slatt, R. 2001).

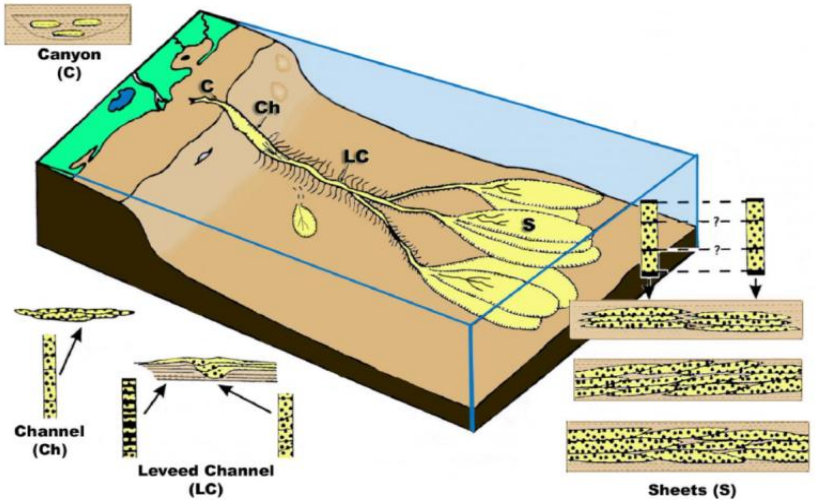

Figure 2.Turbidite reservoir classifications (Slatt, R. 2001).

The Bouma sequence describes the grained variety in sediment-water turbidity current. The Bouma sequence is divided into 5 distinct beds as shown in Figure 3(Shanmugam G. 1997):

e: muds, ungraded after bioturbated.

d: parallel laminated silts.

c: cross laminated sand.

b: parallel laminated sands.

a: sands and any larger grains the turbidity current was carrying at the time of deposition.

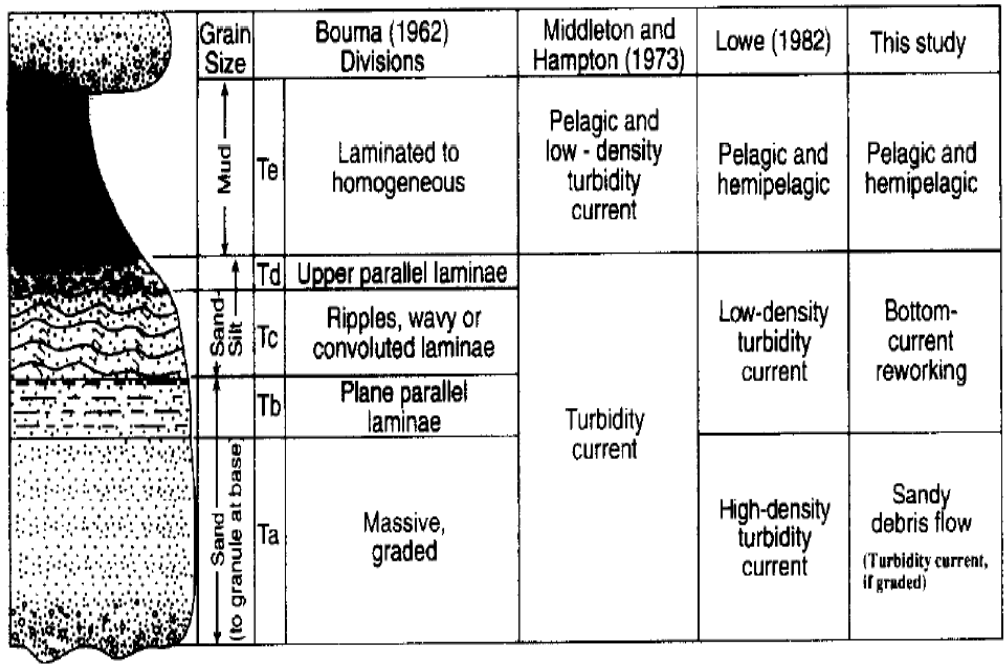

Figure 3.Principal Bouma sequence (Shanmugam G. 1997).

2.2 Fluvial Environment

The term “fluvial” refers to the processes associated with rivers and streams and the deposits and landforms created by them, Figure 4(Knighton, D. 1998). There are two modes for describing the fluvial sediment transportation, Figure 5, (1) suspended load and (2) bedload. Suspended load are the paticles that are continuously floating in the water column, and mostly consist of clay and silt. Bedload refers to larger particles like sand grains and gravels that move along or near the channel bed by traction and saltation.

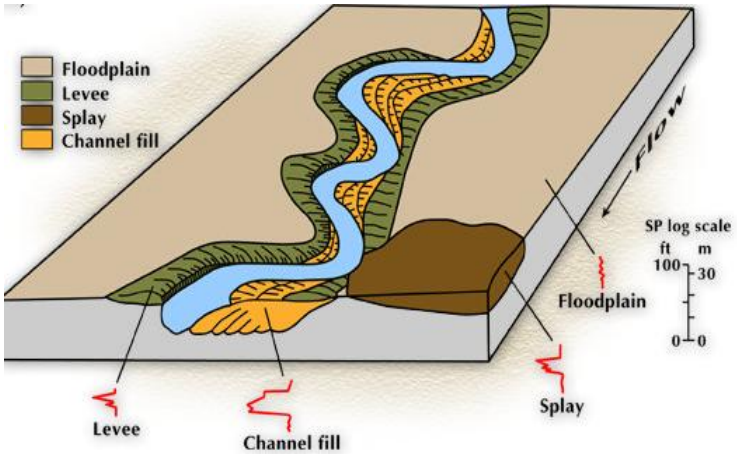

Figure 4.Fluvial system and the interaction of its components (Weber, R., 2010)

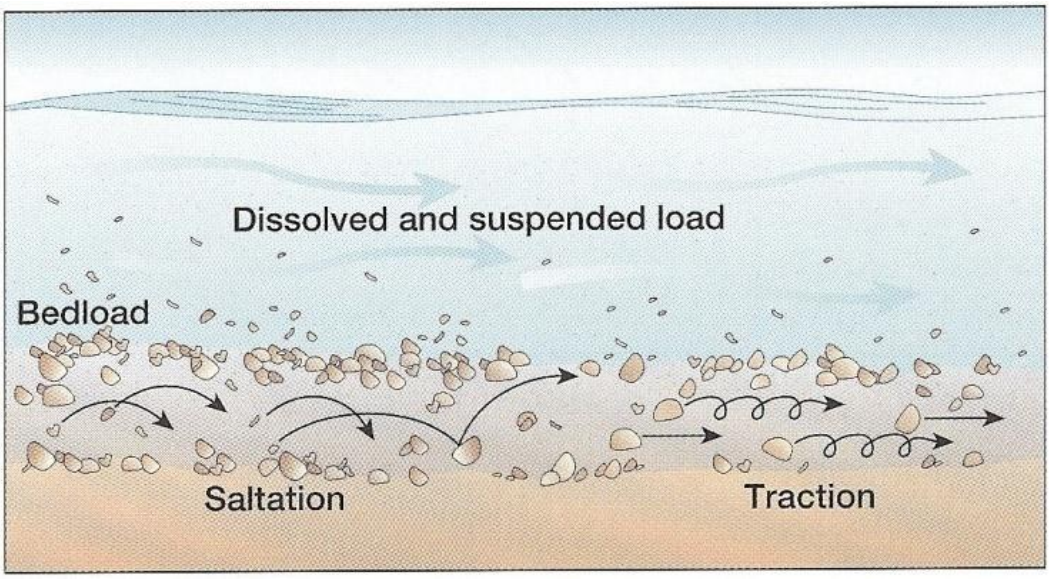

Figure 5.Mechanisms of sediment transport in fluvial systems (Mcknight, T.L., and Hess, D., 2000).

The two case studies in this project are from two different wells drilled in these geological settings, fluvial and turbidite environments, respectively.

CHAPTER 3

Physical Measurements in Open Hole Logs

3.1 Neutron

(Schlumberger, 3rd printing, 1991) Neutron tools emit high energy neutrons and measure the response of these neutrons as they interact with the formation, or in many cases, the fluids within the formation, Figure 6. This measured response is affected by the quantity of neutrons at different energy levels and by the decay rate of the neutron population from one given energy level to another, Figure 7. In well logging, there are four important interactions between a bombarding neutron and a target nucleus as shown in Figure 8. Inelastic neutron scattering occurs when the neutron recoils the nucleus, excites it and quickly give off what are called inelastic gamma rays. Inelastic neutron scattering is possible only if the neutron energy exceeds a characteristic threshold for the element. Neutron Elastic scattering occurs when the neutron recoils the bombarded nucleus without exciting it, but with each elastic interaction, the neutron loses energy. Elastic scattering is the most important reaction for typical porosity logging. Absorption becomes more and more probable as the neutron energy is reduced, and when it occurs the neutron disappears.

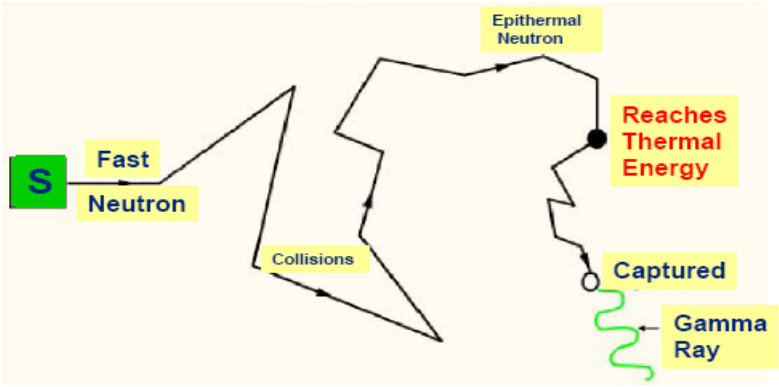

Figure 6.A bombarded-neutron Interacts in a formation (Schlumberger Training Courses).

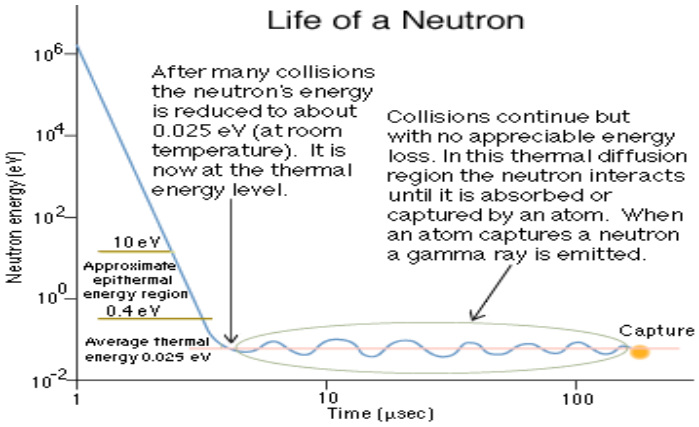

Figure 7.The neutron life in the formation at different energy levels (Schlumberger Training Courses).

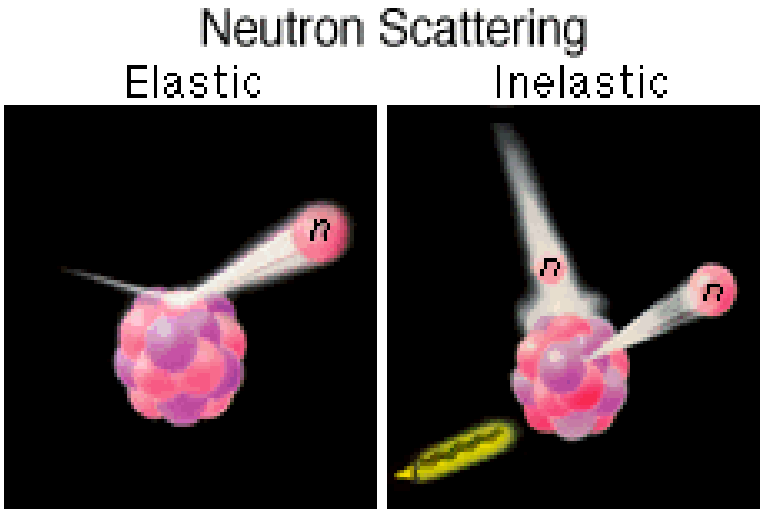

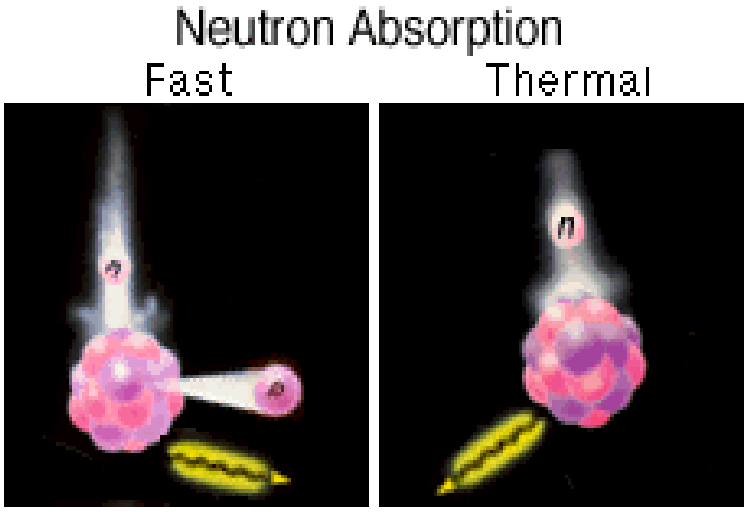

Figure 8.The interactions of a neutron with a target nucleus can be classified as scattering and absorption ((Schlumberger Training Courses).

Hydrogen is the most effective element to cause a neutron to lose energy through elastic scattering due to the fact that its weight mass is the same as that of a neutron. The neutron population at any point during logging depends mainly on the quantity of hydrogen between the source and that point. This is known as the hydrogen index (HI), which is a measure of the quantity of hydrogen per unit volume. High HI means most of the neutrons are slowed and captured within a short distance from the source, and apparently high neutron porosity in the formation. While low HI means the neutrons travel farther from the source before they are captured indicating low neutron porosity in the formation, Figure 9.

Environmental corrections can be applied to the neutron measurements depending on a hole size, mud salinity, mud weight, temperature, and pressure.

Shales have water (hydrogen nuclei) bound in their rock structure and have an appreciable hydrogen index. Therefore, in shaly formations the apparent porosity derived from the neutron response will be greater than the actual effective porosity of the reservoir rock.

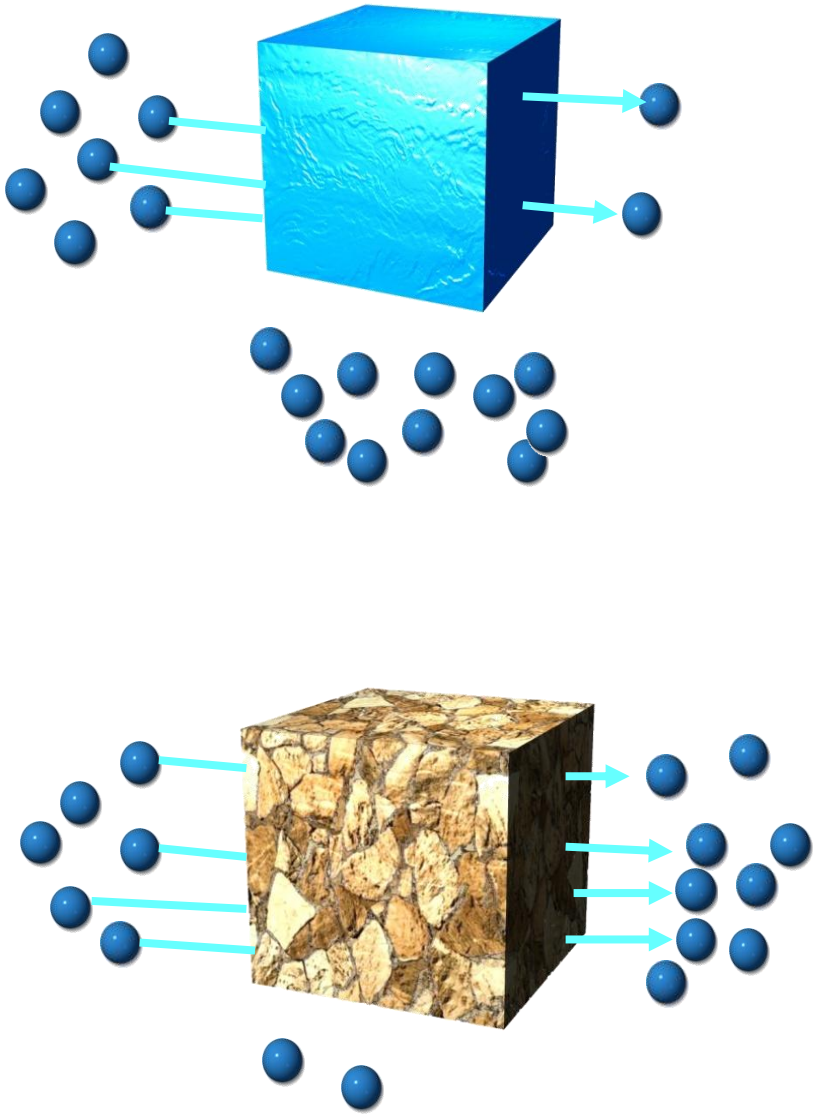

Figure 9.The quantity of the neutrons are more slowed down and captured by the amount of the Hydrogen Index in the formation (Schlumberger Training Courses).

3.2 Density

(Schlumberger, 3rd printing, 1991) Density logging is based on gamma ray interactions in a formation. As gamma rays pass through matter, they experience a loss of energy due to collisions with atomic particles. These collisions can be divided into three basic categories:

Pair Production

It is the conversion of a gamma ray into an electron and positron when the gamma ray enters a strong electric field near an atom's nucleus. It predominates at gamma ray energy levels that are above 10 MeV. There is no application of pair production in the logging measurements.

Compton Scattering

It is the scattering of a gamma ray by an orbital electron. As a result of this interaction, the gamma ray loses energy and an electron is ejected from its orbit. Compton scattering predominates in the 75 keV to 10 MeV energy range.

Photoelectric Absorption

It is the absorption of a (low energy) gamma ray by an orbital electron.

The gamma rays in the Compton scattering processing interact with the electrons in the outer shell of an atom, while in the photoelectric absorption, the gamma rays interact with the inner shell, Figure 10 and Figure 11.

The density log responds to the electron density of the formations. For a molecular substance, the electron density index is related to the bulk density:

$$e_e = e_b * 2(\frac{\sum Z's}{Mol.Wt})$$

e_e= electron density

e_b= bulk density

$\sum Z'$ = the sum of the atomic numbers of atoms making up the molecule.

Mol.Wt = the molecular weight.

$(\frac{\sum Z's}{Mol.Wt})$ ~ 1 for most elements.

Therefore the measured e_e is very close to e_b. when the density tool is calibrated in freshwater-filled limestone formations, the apparent bulk density e_a as read by the tool is related to the electron density index e_e:

$$e_a = 1.0704e_e - 0.1883$$

Practically, the apparent bulk density e_a is identical to the required bulk densitye_b.

The equation that is used to convert the density measurement into formation porosity:

$$\delta_b = \delta_f \phi + \delta_{mat}(1-\phi), sothat$$
$$\phi = \frac{\delta_{ma} - \delta_b}{\delta_{ma} - \delta_{ft}}$$

There are two inputs into the porosity equation: the matrix density and the fluid density. For good approximation, matrix density can be estimated as 2.71 g/cc (limestone density) 2.65 g/cc (sandstone density) or 2.95 g/cc (dolomite density) based on the compatible scale with neutron, while fluid density is taken as water density (~ 1gm/cc).

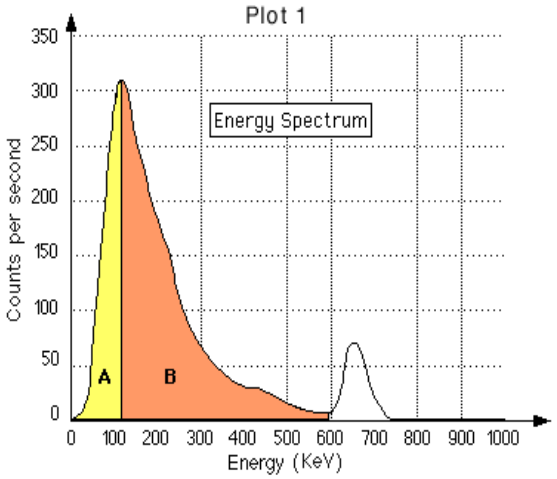

Figure 10.scattering (region B) predominates at high energy level while photoelectric absorption (region A) predominates at low energy level of gamma rays (Schlumberger, 3rd printing, 1991)

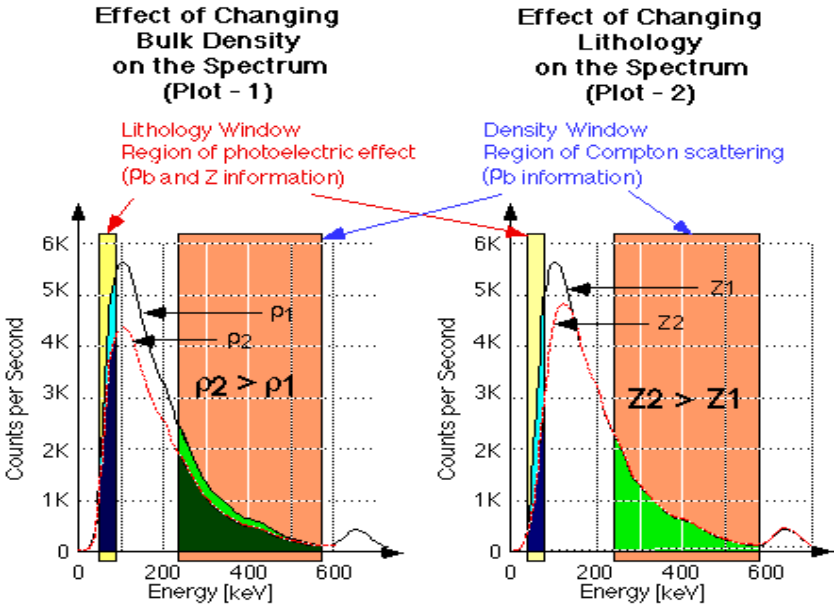

Figure 11.Compton scattering region gives information about changes in bulk density, while photoelectric absorption region gives information for both changes in lithology (atomic number Z) and bulk density.(Schlumberger, 3rd printing, 1991).

3.3 Nuclear Magnetic Resonance

Nuclear Magnetic Resonance refers to the response of nuclei to a magnetic field. Many nuclei have a magnetic moment i.e. in a static magnetic field they behave like spinning bar magnets. These spinning magnetic nuclei interact with external magnetic fields and produce measureable signals. It has been noted that these measureable signals from the nuclei of the hydrogen atoms is maximized compared to other elements, because hydrogen has a relatively large magnetic moment (Akkurt, R. et.al. Oilfield Review Winter2008/2009, Asquith, G., and Krygowski, D., 2004). The measurement sequence starts with the hydrogen proton's alignment by an external magnetic field , followed by spin tipping, precession and repeated dephasing and refocusing, Figure 12. The quantities measured are signal amplitude and decay. This NMR decay (called relaxation) generates information in well logging about pore size distribution in the formation. The distribution of the relaxation times is a measure of the distribution of pore sizes. For example, small pores shorten relaxation times, while large pores correspond to long relaxation times. Relaxation times and their distributions also provide information about permeability, producible porosity and irreducible water saturation. There are two relaxation times of NMR decay signals.One uses longitudinal relaxation T1 and T1 distribution and Transverse relaxation time T2 and T2 distribution. T1 is usually measured with laboratory instruments, while T2 is measured by borehole instruments. Transverse relaxation time T2 is faster than longitudinal relaxation time T1 i.e. $T2<T1$. In addition, T1 measurements are low quality in the boundaries of strongly contrasting beds and they are not repeatable compared to T2 measurements (Kleinberg, R., et al 1993) as shown in Figure 13. T2 measurements are function of pore surface relaxation, bulk relaxation, as

well as diffusion (Akkurt, R. et al Oilfield Review Winter2008/2009, Chinese Science and Technology Papers Online).

Most borehole tools use the CPMG technique to measure T2, wher a complete CPMG sequence has 3000*180 deg pulses and measures 3000 echoes at 200 usec spacing as shown in Figure 14 (Hook, P. et al 2011).

The composite signal of T2 relaxation is inverted, using Laplace transform, and the values are displayed as a histogram that reflect the pore size distribution of the rock, Figure 15. The area under the T2 distribution reflects total NMR porosity , and by applying an appropriate empirical cut-off in the T2-distribution , the NMR total porosity can differentiate between free fluid volumes vs. bound fluid volumes ,Figure 16 and Figure 17.

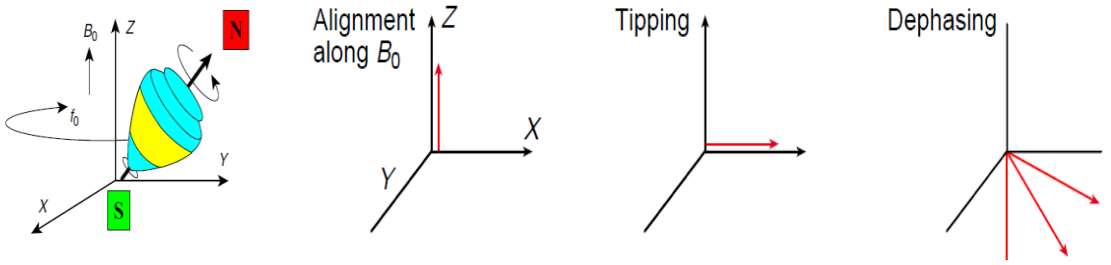

Figure 12.The axis of the spinning H atom precesses around Bo. When tipped out of alignment, hydrogen nuclei behave like a spinning top. Over time, hydrogen nuclei diphase and realign with the static magnetic field (Asquith, G., and Krygowski, D., 2004).

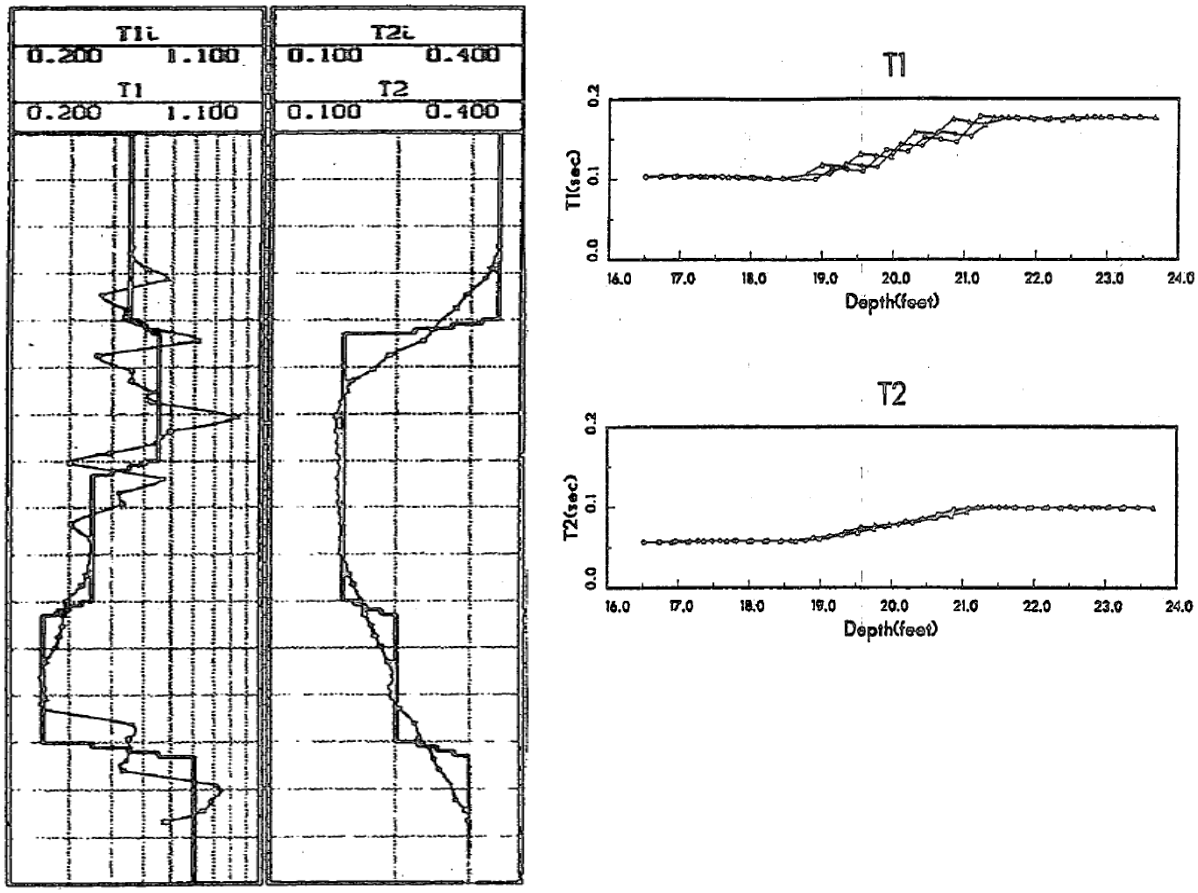

Figure 13.Comparison between T1 and T2 across bedding (left) and repeatability (right) (modified from Kleinberg,,et al. 1993).

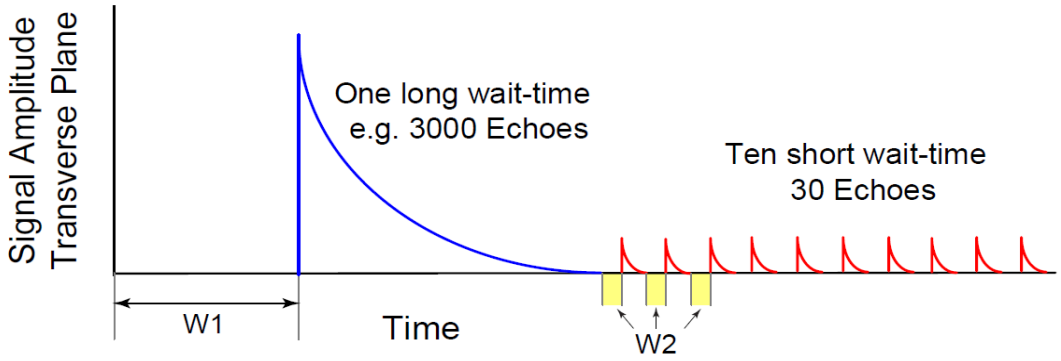

Figure 14.Concept of the exponential signal decay and the echo spacing (modified from Hook, P.,et al 2011).

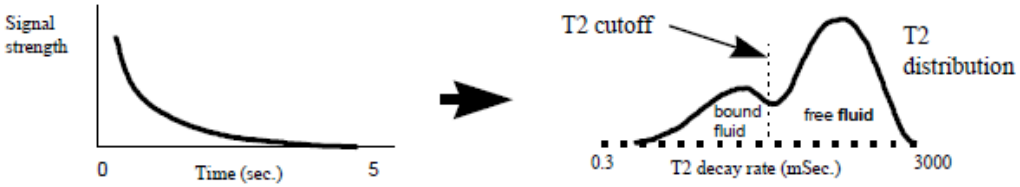

Figure 15.The decay of NMR T2 signale (left) is normally shown as a distribution of all the various decay rates (right) (modified from Akkurt, R. et al Oilfield Review Winter2008/2009).

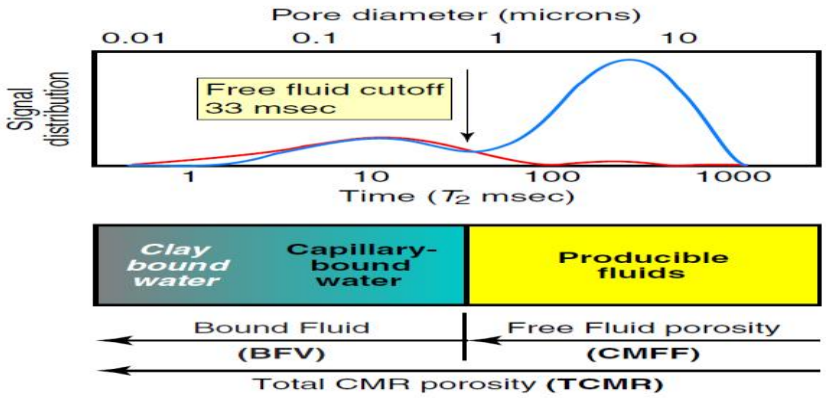

Figure 16.NMR measures TCMR (total porosity) which equals to summation of CMFF (Free Fluid porosity) and BFV. (Bound Fluid = clay bound water + capillary bound water) (modified from Asquith, G., and Krygowski, D., 2004).

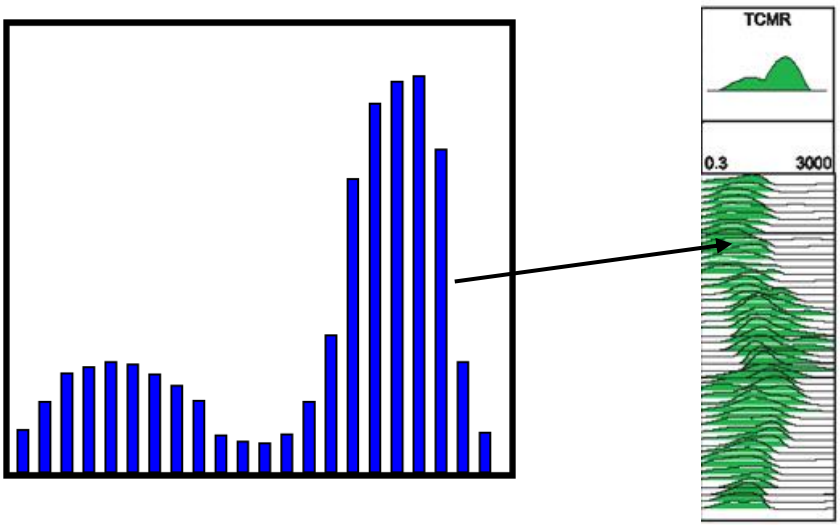

Figure 17.The standard NMR log displays primarily the total porosity and distribution (modified from (Asquith, G., and Krygowski, D., 2004).

3.4 Triaxial Resistivity Induction logs

Electrical anisotropy is defined as changing in electrical properties (Resistivity) with direction. The vertical and horizontal resistivity values of an anisotropic medium are not equal. Shale rocks are common examples of anisotropy. Traditional resistivity tools that consist of aligned Transmitter-Reciever coils perpendicular to the bedding usually respond to the horizontal component of the measured resistivity (Rh), which is parallel to the bedding. For example, Figure 18 shows a simple model composed of coarse grains of sands laminated by shale layers. Assume this model consists of 50% sand and 50% shale with 1Ω.m shale resistivity and 10 Ω.m sand resistivity. The linear conductivity response is:

$\sigma_t = V_{shale} * \sigma_{Shale} + V_{Sand} * \sigma_{sand}$ ..... (1)

V_{shale}= volume fraction of shale.

V_{Sand}= volume fraction of sand.

σ_t= total conductivity measurement.

σ_{Shale}= conductivity measurement of shale.

σ_{sand}= conductivity measurement of sand.

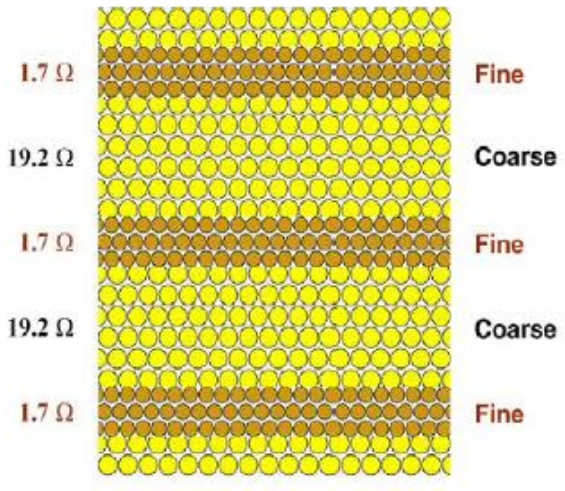

Figure 18.A simple model composed of homogenous fine grains (shales) and coarse grains (sands).

The computed formation resistivity Rt of the above example is 1.81 Ω.m. If the sand resistivity is increased to 100 Ω.m and shale resistivity is left as 1 Ω.m, the computed formation resistivity Rt will be 1.98 Ω.m. Therefore, the formation resistivity Rt is reading around 2 Ω.m even when the sand resistivity is increased to 100 Ω.m. However, if we assume that there is a vertical resistivity Rv, measured perpendicular to layers, besides Rh, the following equations can be applied:

$$\sigma_h = V_{shale} * \sigma_{shale} + V_{sand} * \sigma_{sand} \quad \ldots\ldots (2)$$

$$R_v = V_{shale} * R_{shale} + V_{sand} * R_{sand} \quad \ldots\ldots (3)$$

$$V_{sand} + V_{shale} = 1 \quad \ldots\ldots (4)$$

These equations are known as Klein equations (Minh, C. et al, 2007), after Jim Klien who first published them.

Returning to the previous hypothetical 50 % sand and 50 % shale example, and computing Rv and Rh from equations 2-4, we get the results listed in the table:

R_{shale}	R_{sand}	R_h	R_v
1 Ω-m	10 Ω-m	1.81 Ω-m	5.5 Ω-m
1 Ω-m	100 Ω-m	1.98 Ω-m	50.5 Ω-m

When Rsand was 10 Ω-m, Rv was 5.5 Ω-m, but when Rsand was increased to 100 Ω-m, Rv has become 50.5 Ω-m. The difference in Rv values reveals too much more uncertainty. The question arises: How is Rv measured?

The Triaxial induction tool is an advanced induction tool that measures 3×3 tensor magnetic field responses in a borehole environment. It consists of three orthogonal transmitters and three orthogonal receivers oriented at x, y and z direction. The tool can be simplified as coils that are usually treated as magnetic dipoles. Figure 19 shows a simple model of the main components of this tool. For every logging point along the borehole axis, a 3×3 magnetic field tensor H is measured at the receiver.

The responses between transmitters and receivers at the same orientation (σxx, σyy, σzz) and those that at the cross-couplings between orthogonal transmitters and receivers (σxy, σxz, σyx, σyz, σzx, σzy) are measured simultaneously at the same depth.

These nine component raw array data is transformed via 1D inversion, into Rv, Rh, dip & bed boundaries Figure 20 (Claverie, M. et al 2006; Kriegshäuser, B., et al. 2000, Zhang, Z. et al. Unvi. of Huston).

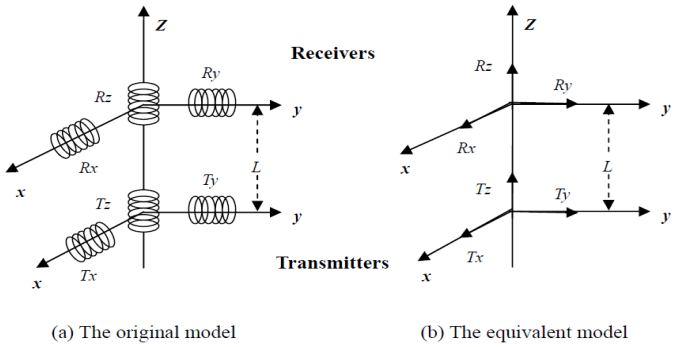

Figure 19.A simplified model showing the setup of the Triaxial resistivity tool (Zhang,Z. et al. Unvi. of Huston)

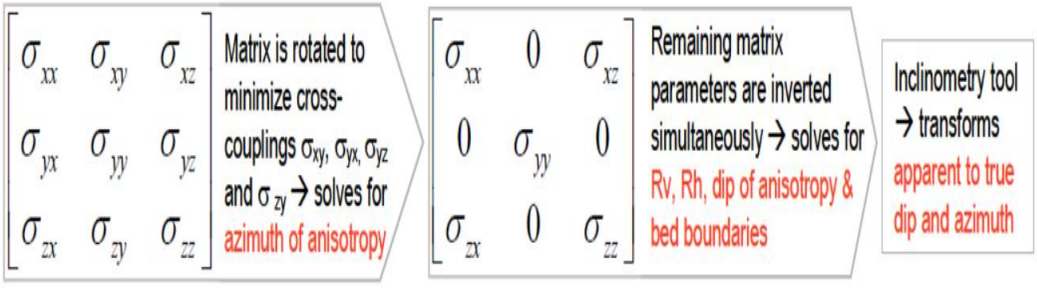

Figure 20.1D-inversion algorithm to generate Rv and Rh (Claverie, M. et al 2006)

The measured Rv & Rh then are used as inputs in Klein equation (2-4). Assuming Rshale is known; those equations can be inverted to yield:

$$R_{sand} = R_h * \frac{(R_v - R_{shale})}{(R_h - R_{shale})} \quad \text{.....(5)}$$

$$F_{sand} = \frac{(R_v - R_{shale})}{(R_{sand} - R_{shale})} \quad \text{.....(6)}$$

$$F_{shale} = 1 - F_{sand} \quad \text{.....(7)}$$

However, shales themselves exhibit anisotropy that increase with compaction (Cook J. 1993). Therefore, two independent parameters R_{shh} &R_{shv}, representing horizontal and vertical shale resistivity respectively, are considered if the shale is anisotropic.

Inserting these two parameters ($\mathbf{R_{shh}}$ &$\mathbf{R_{shv}}$) into Klein equations (2-4) will create a system of isotropic sand- anisotropic shale as shown in Figure 21, which is called advanced Klein equations or Clavaud equations (Minh, C. et al, 2007) as following:

$$R_v = F_{sand} * R_{sand} + F_{sh\_Lam} * R_{shv} \quad \text{..... (8)}$$

$$\frac{1}{R_h} = \frac{F_{sand}}{R_{sand}} + \frac{F_{sh\_Lam}}{R_{shh}} \quad \text{..... (9)}$$

$$1 = F_{sand} + F_{sh\_Lam} \quad \text{..... (10)}$$

R_v= Vertical resistivity component

R_h = Horizontal resistivity component

F_{sand}, R_{sand} = Volume fraction of sand and resistivity measurement of sand, respectively.

F_{sh_Lam} = Volume fraction of laminated shale in sand facies

R_{shv} = Vertical resistivity component of shale

R_{shh}= Horizontal resistivity component of shale

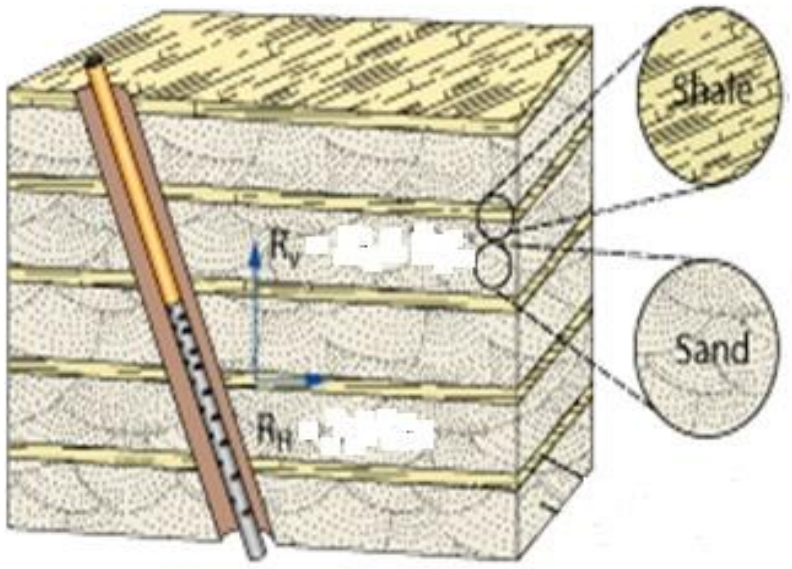

Figure 21.Schemetic of isotropic sand-anisotropic shale with respect to tool response (Clavaud, J., et al. 2005).

The introduction of shale anisotropy (R_{shh} & R_{shv}) complicate the simple Klein bimodal resistivity model. The inversion for the true sand resistivity (R_{sand}) and hence water saturation in the sand facies from equations (8-10), is illustrated in the following interpretation steps:

1) Compute the formation evaluation based on the open hole logs to solve for total porosity$\emptyset_T$, and volume of ClayV_{cl}.

2) From an adjacent massive shale zone, the two shaly anisotropic parameters (R_{shh}, R_{shv}) and $\emptyset_{sh}$ are chosen or a sliding window is used (Hayden, R. et al 2009).The shale anisotropy α equalsR_{shv}/R_{shh}.

3) The solution of equations 8 through 10 gives:

$$R_{shh} = \frac{R_v - R_h*(1-F_{sh\_lam})^2 + \alpha*R_h*F_{sh\_lam}^2 \pm \sqrt{\left[R_v + R_h*\left(F_{sh_{lam}}*(1-\alpha)-2\right)+1\right)]^2 - 4*(1-F_{sh_{lam}})^2*R_h*R_v}}{2*\alpha*F_{sh\_lam}} \quad \text{(11)}$$

$$\mathbf{R_{sand} = \frac{R_v + R_h*(1-F_{sh\_lam})^2 - \alpha*R_h*F_{sh\_lam}^2 \pm \sqrt{[R_v + R_h*(F_{sh\_lam}*(1-\alpha)-2)+1)]^2 - 4*(1-F_{sh\_lam})^2*R_h*R_v}}{2*\alpha*F_{sh\_lam}}}. \quad (12)$$

The sign ($\pm$)in equations (11) and (12) is determined based on a cut-off value for R_{shh} compared to a given $R_{h\text{-}limit}$ (Clavaud, J., et al. 2005).

$$R_{h\_limit} = \frac{R_{shh}^2}{F_{shh}*\alpha*R_{shh} + R_{shh}*\sqrt{\alpha*(1-F_{sh})^2}} \quad (13)$$

When $R_h >= R_{h\_limit}$

$$\mathbf{R_{sand}} = \frac{\mathbf{R_v + R_h*(1-F_{sh\_lam})^2 - \alpha*R_h*F_{sh\_lam}^2 + \sqrt{[R_v + R_h*(F_{sh\_lam}*(1-\alpha)-2)+1)]^2 - 4*(1-F_{sh\_lam})^2*R_h*R_v}}}{\mathbf{2*\alpha*F_{sh\_lam}}} \quad (14)$$

$$\mathbf{R_{shh}} = \frac{\mathbf{R_v - R_h*(1-F_{sh\_lam})^2 + \alpha*R_h*F_{sh\_lam}^2 - \sqrt{\left[R_v + R_h*\left(F_{sh_{lam}}*(1-\alpha)-2\right)+1\right)]^2 - 4*(1-F_{sh_{lam}})^2*R_h*R_v}}}{\mathbf{2*\alpha*F_{sh\_lam}}} \quad (15)$$

Otherwise;

$$\mathbf{R_{sand}} = \frac{\mathbf{R_v + R_h*(1-F_{sh\_lam})^2 - \alpha*R_h*F_{sh\_lam}^2 - \sqrt{[R_v + R_h*(F_{sh\_lam}*(1-\alpha)-2)+1)]^2 - 4*(1-F_{sh\_lam})^2*R_h*R_v}}}{\mathbf{2*\alpha*F_{sh\_lam}}} \quad (16)$$

$$\mathbf{R_{shh}} = \frac{\mathbf{R_v - R_h*(1-F_{sh\_lam})^2 + \alpha*R_h*F_{sh\_lam}^2 + \sqrt{\left[R_v + R_h*\left(F_{sh_{lam}}*(1-\alpha)-2\right)+1\right)]^2 - 4*(1-F_{sh_{lam}})^2*R_h*R_v}}}{\mathbf{2*\alpha*F_{sh\_lam}}} \quad (17)$$

If the term within the square root is computed as negative value, then the value chosen for α was too high. The value of α in such circumstances will be adjusted to make the term within the square root equal to zero. This new value of $\alpha 2$ is recomputed as:

$$\alpha 2 = (-2 * ((F_{sh_{lam}} - 1)^2 * F_{sh\_lam}^4 * R_h^3 * R_v)^{0.5} + F_{sh\_lam}^2 * R_h * ((F_{sh} - 1)^2 * R_h + R_v))/(F_{sh\_lam}^4 * R_h^2) \quad (18)$$

Practically, we should first check whether the square root term (Radical) is not negative, otherwise use $\alpha 2$.

4) The total fraction of shale (F_{sh}) is computed as $F_{sh} = V_{cl}/(1\text{-}\emptyset_T)$. Then, the volume fraction of dispersed shale in the sand facies is taken into account by subtracting F_{sh_Lam} from the fraction of total shale F_{sh}as $F_{shale\_Disp} = F_{sh} - F_{sh\_Lam}$.

5) By assuming $\emptyset_{sh\_lam}$ is equal to $\emptyset_{sh}$ that was computed in step 2, the porosity in the sand fraction is computed as :

$$\emptyset_{sand} = \frac{\emptyset_T - F_{sh\_Lam} * \emptyset_{sh}}{F_{sand}} \quad (19)$$

$\emptyset_T$ = Total porosity.

$\emptyset_{sh}$ = porosity volume of the shale layers.

F_{sh_Lam} = Volume fraction of laminated shale in sand facies.

The computed sand porosity from equation 21 includes the dispersed pore filling shale. To compute the effective sand porosity, this dispersed part must be excluded from the sand facies. The clay water fraction in the dispersed clay is computed by multiplying the total clay bound water v_{xbw} by the ratio of dispered shale to total shale and normalizing to the sand fraction (Hayden, R., et al. 2009).

$$\emptyset_{dis\_clay} = \frac{V_{xbw} * F_{sh\_disp}}{F_{shale} * F_{sand}} \quad (20)$$

The effective sand porosity is the clay bound water fraction associated with the dispersed clay subtracted from the total porosity in the sand facies:

$$\emptyset_{sand\_eff} = \emptyset_{sand} - \emptyset_{disp\_clay} \quad (21)$$

6) Compute total water saturation in the sand fraction $S_{w_{sand}}$ using Dual-water Equation (Clavier, C., 1977) or Waxman-Smits Equation (Devarajan, S. et al 2006), and the effective water saturation in the sand facies is computed by subtracting dispersed clay bound water from total water volume in the sand fraction divided by $\emptyset_{sand\_eff}$.

3.5 The Thomas-Stieber Plot

Thomas, E. and Stieber, S., in 1975 tried to find a method to determine shale distribution in the sand particles, sand fractions and the sand porosity. This method was developed based on the gamma ray responses along with total porosity measurements. (Thomas E., and Stieber S. 1975)

The authors made the following assumptions for a sand-shale model:

1. A model consists only of high porosity "clean" sand and low porosity "pure" shale.

2. No significant change in the shale type and texture when mixed with sands.

3. The gamma ray response will be affected only by the radioactive events in a material , mainly associated with clay minerals.

4. No change in the counting rates, or radiations, at all measurements, and no change in the counting yields as rock types are intermixed.

5. Structural shale configurations in the sands are insignificant.

The following derivations explain the development of Thomas-Stieber graph.

For zero-porosity clean sand, the gamma-ray counting rate R^*_{sd} is:

$$R^*_{sand} = Y_{sd} * A_{sd} \quad \ldots\ldots (1)$$

Y_{sd}= counting yield

A_{sd}= sand activity

Crushing the sand material and introduce void space in the sand, the count rate then can be expressed as:

$$\mathrm{R_{sd}} = (1 - \emptyset_{\mathrm{sd}}) * \mathrm{Y'_{sd}} * \mathrm{A_{sd}} \ldots\ldots\ldots\ldots\ldots\ldots\ldots\ldots\ldots\ldots\ldots\ldots\ldots (2)$$

Y'_{sd}= the new counting yield after crushing sand.

$\emptyset_{sd} =$ Sand porosity

Repeating the same experiment on the shale material, the counting rate can be expressed as:

$$\mathrm{R_{sh}} = (1 - \emptyset_{\mathrm{sh}}) * \mathrm{Y'_{sh}} * \mathrm{A_{sh}} \ldots\ldots\ldots\ldots\ldots\ldots\ldots\ldots\ldots\ldots\ldots\ldots\ldots\ldots (3)$$

$R_{sh} =$ Counting rate of the shale

$\emptyset_{sh}$= shale porosity

Y_{sh}= counting yield of the shale

$A_{sh} =$ shale activity.

By mixing the two materials (porous sand and shale) and assume the counting yields are not changing significantly (assumption No. 4), the counting rate can be expressed based on the shale distribution in the sand Figure 22, as dispersive, laminated, or both of them. (Assumption No.5 ignores structure distribution).

1) **Dispersed Shale:**

The shale particles replace the pore space of the sand. The counting gamma rays can be expressed as

$$R = (1 - \emptyset_{sd}) * Y'_{sd} * A_{sd} + X_{sh,dis} * (1 - \emptyset_{sh}) * Y'_{sh} * A_{sh} \ldots\ldots\ldots\ldots (4)$$

$X_{sh,dis}$ = Total shale fraction in the sand pore space.

Substituting (2) and (3) into (4)

$$R = R_{sd} + X_{sh,dis} * R_{sh} \ldots\ldots\ldots\ldots\ldots\ldots\ldots\ldots\ldots\ldots\ldots\ldots (5)$$

By defining the parameter γ as the sand fraction:

$$\gamma = \frac{R_{sh} - R}{R_{sh} - R_{sd}} \ldots\ldots\ldots\ldots\ldots\ldots\ldots\ldots\ldots\ldots\ldots\ldots\ldots\ldots\ldots\ldots\ldots\ldots (6)$$

Substituting (5) into (6):

$$\gamma = \frac{R_{sh} - R_{sd} - X_{sh,dis} * R_{sh}}{R_{sh} - R_{sd}} = \frac{(R_{sh} - R_{sd}) - (X_{sh,dis} * R_{sh})}{R_{sh} - R_{sd}}$$

$$= \frac{R_{sh} - R_{sd}}{R_{sh} - R_{sd}} - \frac{X_{sh,dis} * R_{sh}}{R_{sh} - R_{sd}}$$

$$\gamma = 1 - \frac{X_{sh,dis} * R_{sh}}{R_{sh} - R_{sd}} \ldots\ldots\ldots\ldots\ldots\ldots\ldots\ldots\ldots\ldots\ldots\ldots\ldots\ldots\ldots\ldots\ldots\ldots (7)$$

For simplicity, we define another parameter ε;

$$\varepsilon = \frac{R_{sh}}{R_{sh} - R_{sd}} \ldots\ldots\ldots\ldots\ldots\ldots\ldots\ldots\ldots\ldots\ldots\ldots\ldots\ldots\ldots\ldots\ldots\ldots (8)$$

Solve equation (7) for $X_{sh,dis}$:

$$1 - \gamma = \frac{X_{sh,dis} * R_{sh}}{R_{sh} - R_{sd}}$$

$$(1 - \gamma) * (R_{sh} - R_{sd}) = X_{sh,dis} * R_{sh}$$

$$X_{sh,dis} = \frac{1 - \gamma}{\varepsilon} \ldots\ldots\ldots\ldots\ldots\ldots\ldots\ldots\ldots\ldots\ldots\ldots\ldots\ldots\ldots\ldots\ldots\ldots\ldots\ldots (9)$$

If we start with the clean sand porosity $\emptyset_{sd}$ and then add shale in the pore spaces of the sand, the dispersed sand porosity ($\emptyset_{\mathrm{dis\_sd}}$) becomes:

$$\emptyset_{\mathrm{dis\_sd}} = \emptyset_{sd} - \mathrm{X}_{\mathrm{sh,dis}} * (1 - \emptyset_{\mathrm{sh}}) \text{ ....} (10)$$

Substitute (9) into (10):

$$\emptyset_{\mathrm{dis\_sd}} = \emptyset_{sd} - \frac{(1-\gamma)*(1-\emptyset_{\mathrm{sh}})}{\varepsilon}$$

When $X_{sh,dis} = 0 \Rightarrow \gamma = 1 \Rightarrow \emptyset_{\mathrm{dis\_sd}} = \emptyset_{\mathrm{sd}}$ ………………………………(11)

When $\mathrm{X}_{\mathrm{sh,dis}} = \emptyset_{sd} \Rightarrow \emptyset_{\mathrm{dis\_sd}} = \emptyset_{sd} * \emptyset_{sh}$ (when the shale completely occupies the pore volume of sand)……………..……………………………………..(12)

2) Laminated Shale:

Both the matrix and porosity of sands are replaced by shale particles. The counting rate of the gamma rays can be expressed as:

$$R = (1-\emptyset_{sd}) * Y'_{sd} * A_a - (1-\emptyset_{sd}) * Y'_{sd} * A_{sd} * X_{sh,lam} + (1-\emptyset_{sh}) * Y_{sh} * A_{sh} * X_{sh,lam} \text{..} (13)$$

$X_{sh,lam}$ = Total shale fraction in the lamination.

Substituting (2) & (3) into (13):

$$R = R_{sd} + X_{sh,lam} * (R_{sh} - R_{sd}) \text{…………………………………………..…} (14)$$

From the definition of γ in equation (6):

$$\gamma = \frac{R_{sh} - R_{sd} - X_{sh,lam} * (R_{sh} - R_{sd})}{R_{sh} - R_{sd}} \Rightarrow \gamma = 1 - X_{sh,lam} = X_{sd} \text{ (sand fraction)..} (15)$$

When the shale porosity and grainosity (fractional grain content) replace the porosity and grainosity of sand fractions, the laminated sand porosity $\emptyset_{sd,lam}$ gets

$$\emptyset_{sd,lam} = \emptyset_{sd} - X_{sh,lam} * \emptyset_{sd} + X_{sh,lam} * \emptyset_{sh} \text{ ....} (16)$$

Substituting (15) into (16)

$$\emptyset_{sd,lam} = \emptyset_{sd} - (1-\gamma) * \emptyset_{sd} + (1-\gamma) * \emptyset_{sh}$$

$$\emptyset_{sd,lam} = \emptyset_{sd} - \emptyset_{sd} + \gamma * \emptyset_{sd} + (1-\gamma) * \emptyset_{sh}$$

$$\therefore \emptyset_{sd,lam} = \gamma * \emptyset_{sd} + (1-\gamma) * \emptyset_{sh} \ldots\ldots\ldots\ldots\ldots\ldots\ldots\ldots \text{(17)}$$

3) Sand with Dispersed Shale and Shale laminations:

For the more general case of sand with dispersed shale interlayered with laminated shale,

$\mathrm{X_{sh,dis}}$ is the dispersed shale fraction, defined as:

$$\mathrm{X_{sh,dis}} = \frac{V_{sh,d}}{V_{sd,lam}}$$

$V_{sh,d}$ is the bulk volume of dispersed shale.

$V_{sd,lam}$ is the bulk volume of sand lamination.

$\frac{\mathrm{N}}{\mathrm{G}}$ is the Net to Gross ratio, defined as:

$$\frac{N}{G} = \frac{bulk\ volume\ of\ sand\ laminations}{total\ bulk\ volume}$$

For such combination between sand and shale, we can write:

$$R = N/G[R_{sd} + X_{sh,d}R_{sh}] + (1 - N/G)R_{sh}$$

From the definition of γ in equation (6) ($\gamma = \frac{\mathrm{R_{sh}-R}}{\mathrm{R_{sh}-R_{sd}}}$)

$$\gamma = \frac{R_{sh} - \frac{N}{G}\left(R_{sd} + X_{sh,dis} * R_{sh}\right) - \left(1 - \frac{N}{G}\right) * R_{sh}}{R_{sh} - R_{sd}}$$

$$\gamma = \frac{R_{sh}\frac{N}{G} - \frac{N}{G}R_{sd} - \frac{N}{G} * X_{sh,dis} * R_{sh}}{R_{sh} - R_{sd}} = \frac{R_{sh}\frac{N}{G} - \frac{N}{G}R_{sd}}{R_{sh} - R_{sd}} - \frac{\frac{N}{G} * X_{sh,dis} * R_{sh}}{R_{sh} - R_{sd}}$$

From equation (8), $\varepsilon = \frac{\mathrm{R_{sh}}}{\mathrm{R_{sh}-R_{sd}}}$

$$\therefore\ \gamma = \frac{N}{G}(1 - \varepsilon X_{sh,dis}) \ldots\ldots\ldots\ldots\ldots\ldots \text{(18)}$$

We need to solve for $\frac{\mathrm{N}}{\mathrm{G}}$ and total porosity in the dispersed sand layers ($\emptyset_{\mathrm{dis\_sd}}$) giving the two known measurements total porosity ($\emptyset_t$) and Gamma ray responses.

The total porosity $\emptyset_t$ is:

$\emptyset_t = \frac{N}{G} * \left[\emptyset_{sd} - X_{sh,dis} * (1 - \emptyset_{sh})\right] + (1 - \frac{N}{G}) * \emptyset_{sh}$; solve for $X_{sh,dis}$:

$$X_{sh,dis} = \frac{\frac{N}{G} * \emptyset_{sd}}{\frac{N}{G}(1 - \emptyset_{sh})} - \frac{\emptyset_t}{\frac{N}{G} * (1 - \emptyset_{sh})} + \frac{\emptyset_{sh}}{\frac{N}{G} * (1 - \emptyset_{sh})} - \frac{\emptyset_{sh} * \frac{N}{G}}{\frac{N}{G} * (1 - \emptyset_{sh})}$$

$X_{sh,dis} = \frac{\emptyset_{sd} - \emptyset_{sh}}{1 - \emptyset_{sh}} - \frac{\emptyset_t - \emptyset_{sh}}{1 - \emptyset_{sh}} * \frac{1}{\frac{N}{G}}$, substitute this value of $X_{sh,dis}$ into equation (18), and solve for $\frac{N}{G}$

$$\frac{N}{G} = \frac{\frac{\emptyset_t - \emptyset_{sh}}{1 - \emptyset_{sh}} - \frac{\gamma}{\varepsilon}}{\frac{\emptyset_{sd} - \emptyset_{sh}}{1 - \emptyset_{sh}} - \frac{1}{\varepsilon}} \quad \text{..... (19)}$$

Using equation (19) with equation (18) to solve for$X_{sh,dis}$:

$$X_{sh,dis} = \frac{1 - \frac{\gamma}{N/G}}{\varepsilon}$$

The total porosity in the sand layers ($\emptyset_{\mathrm{dis\_sd}}$) can be evaluated as:

$\emptyset_{\mathrm{dis\_sd}} = \emptyset_{sd} - X_{sh,dis} * \emptyset_{sh}$ ..... (20)

Practically, we have the total porosity and gamma ray measurements and need to solve for $\frac{N}{G}$ and $\emptyset_{\mathrm{dis\_sd}}$ from equation 19 and 20 respectively.

Figure 23 shows the graphical solution to determine sand fraction($\frac{N}{G}$) and total dispersed sand porosity from the two known measurements, total porosity ($\emptyset_t$) and Gamma ray responses. First, we need to determine properly the end points in case of 100% sand and 100% shale. Then, determine the minimum value of sand filled totally with dispersed

shale (equation 12). Solutions can be found for$(\frac{N}{G})$ and sand porosity for any value of gamma ray and the corresponding total porosity readings. This graph is called Thomas and Stieber plot.

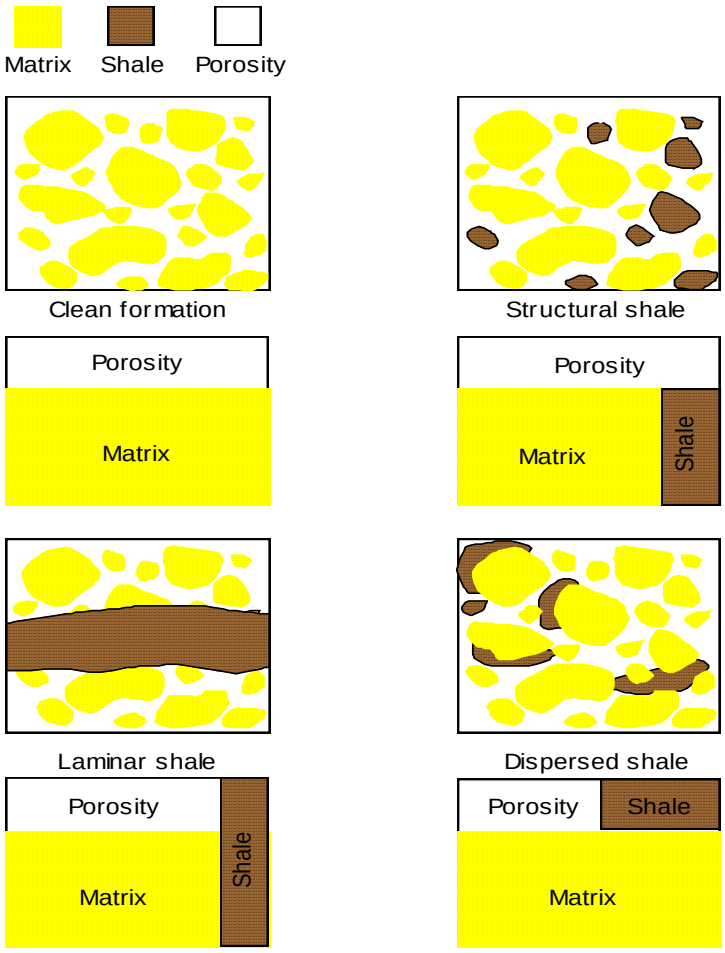

Figure 22.Shale distribution in sand matrix (Pedersen, B.K., and Nordal,K,1999)

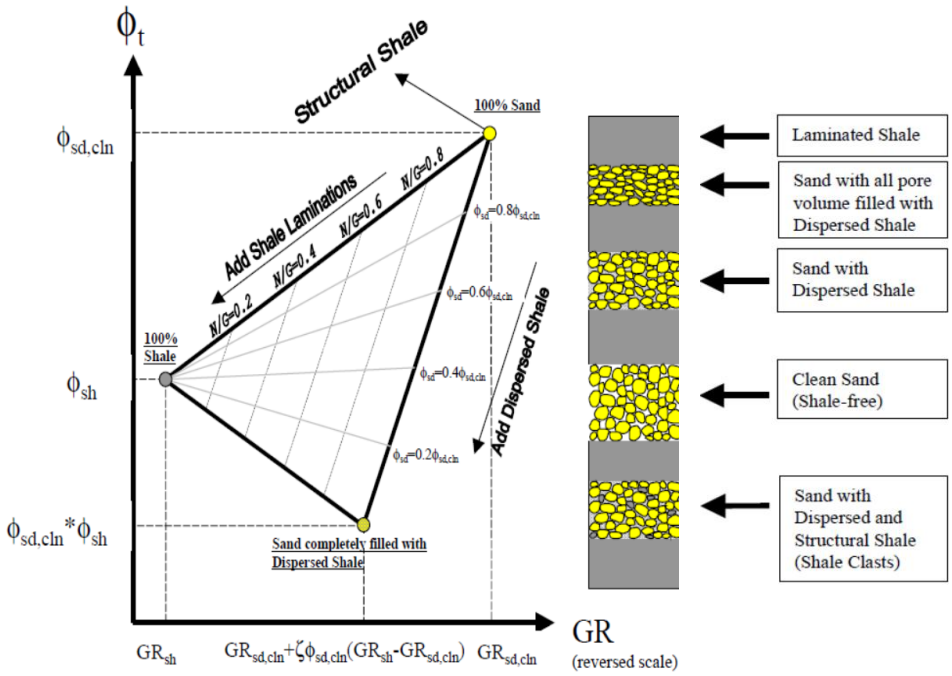

Figure 23.Graphical interpretation of Thomas-Stibier method (Pedersen, B.K., and Nordal,K,1999).

3.6 Electrical Borehole Images

Electrical borehole image tools measure the formation microconductivity directly through an array of electrode buttons that are pressed against the borehole wall. From these microconductivity measurements, an image is generated that shows bedding , fractures and other geological features, as in Figure 24.

The images are presented as functions of azimuth and depth starting at an azimuth of zero (North) moving clockwise to East 90°, south 180°, West 270° and back to 360° North. These high vertical resolution images are displayed in colors ranging from more dark (conductive) to white or beige (resistive). Fractures intersecting boreholes appear in the image as sinusoids. The amplitude of the sine wave corresponds to a dip angle, and its phase corresponds to an azimuth, as shown in Figure 25. The interpretation from electrical borehole images should be combined with other petrophysical logs (resistivity, neutron and density) and available cores to provide detailed sedimentary facies (Joubert J. and Maitan, V., 2010, Hansen, S.M., and Fett,T.,1998).

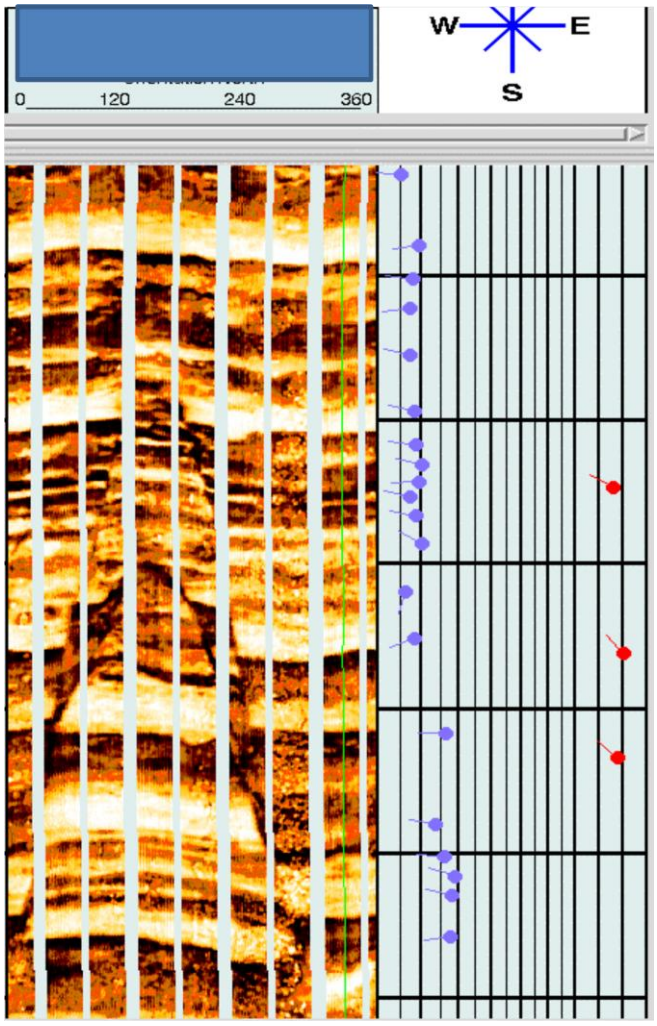

Figure 24.Track 1 is the borehole image generated from microresistivity measurements. Track2 is the corresponding geological features in tadpole forms. (Hansen, S.M., and Fett,T,1998)

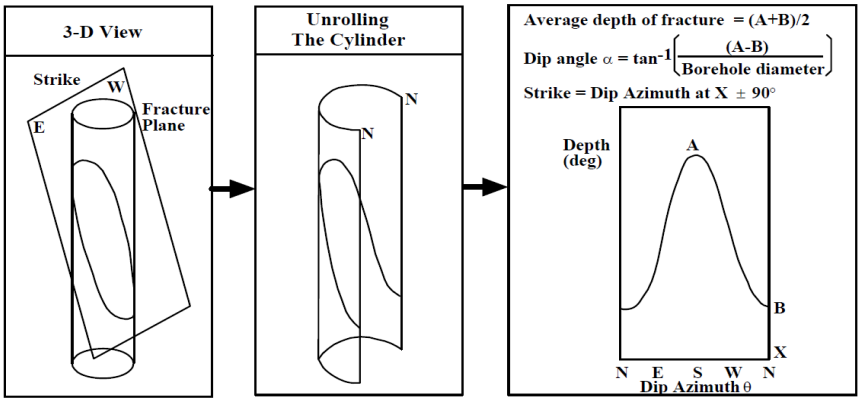

Figure 25.planar surfaces such as bedding planes, faults etc are shown as sine waves (Hansen, S.M., and Fett,T,1998).

The vertical resolution of the conventional logs (Neutron-Density-Resistivity) is insufficient to accurately detect true petrophysical properties of each bed in a sand-shale lamination sequence. However, the borehole images can measure the micro-resistivity of each bed as thin as 1 cm (Kantaatmadja, B. et al. 2010), Figure 26.

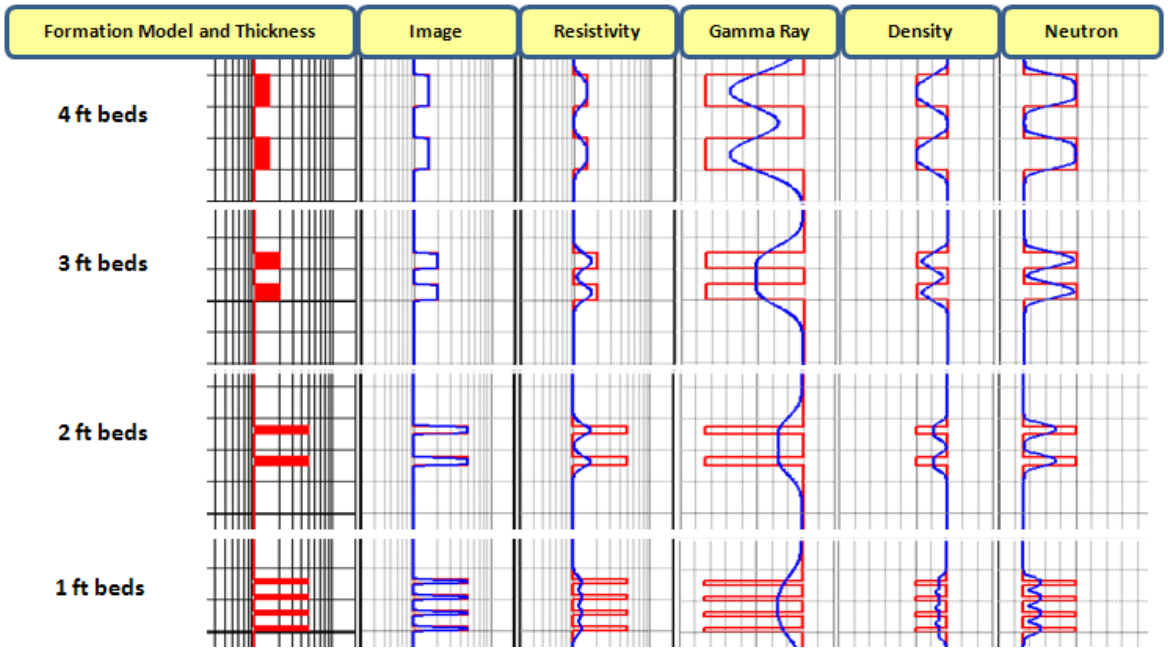

Figure 26.Vertical resolutions for most open hole logs. Blue curve is measured, and red one is the true formation properties. (Kantaatmadja B. et al 2010)

3.7 Deconvolution Techniques using Image Logs

SHARP processing (Yadav, L. et al 2012, and Bastia, R., et al. 2007) is a method of combining open hole logs (Neutron-Density-Resistivity) with borehole images to interpret a laminated sand-shale sequence and provides a very high resolution formation evaluation and interpretation for each thin bed properties.

The high resolution micro-resistivity curve from the image (SRES) is squared and combined with a standard formation evaluation from the conventional logs or NMR to create a layered earth resistivity model consisting of a set of beds or lithofacies named as sand, silt, shale, wet and tight, Figure 27. These lithofacies are determined by applying appropriate cut-offs on the squared resistivity curve, such that, the earth resistivity model should have initial property values similar to the thick beds in the standard formation evaluation. The predicted log responses from each bed in the model are simulated to be matched with their respective measured logs. The lithofacies are adjusted until the predicted and measured logs are matching. This process is called 1D Thin Bed Analysis Convolution. Based on this analysis, an initial set of squared logs are created for the open hole logs. These squared logs are then used as inputs in a petrophysical interpretation program to recompute the formation evaluation, Figure 28.

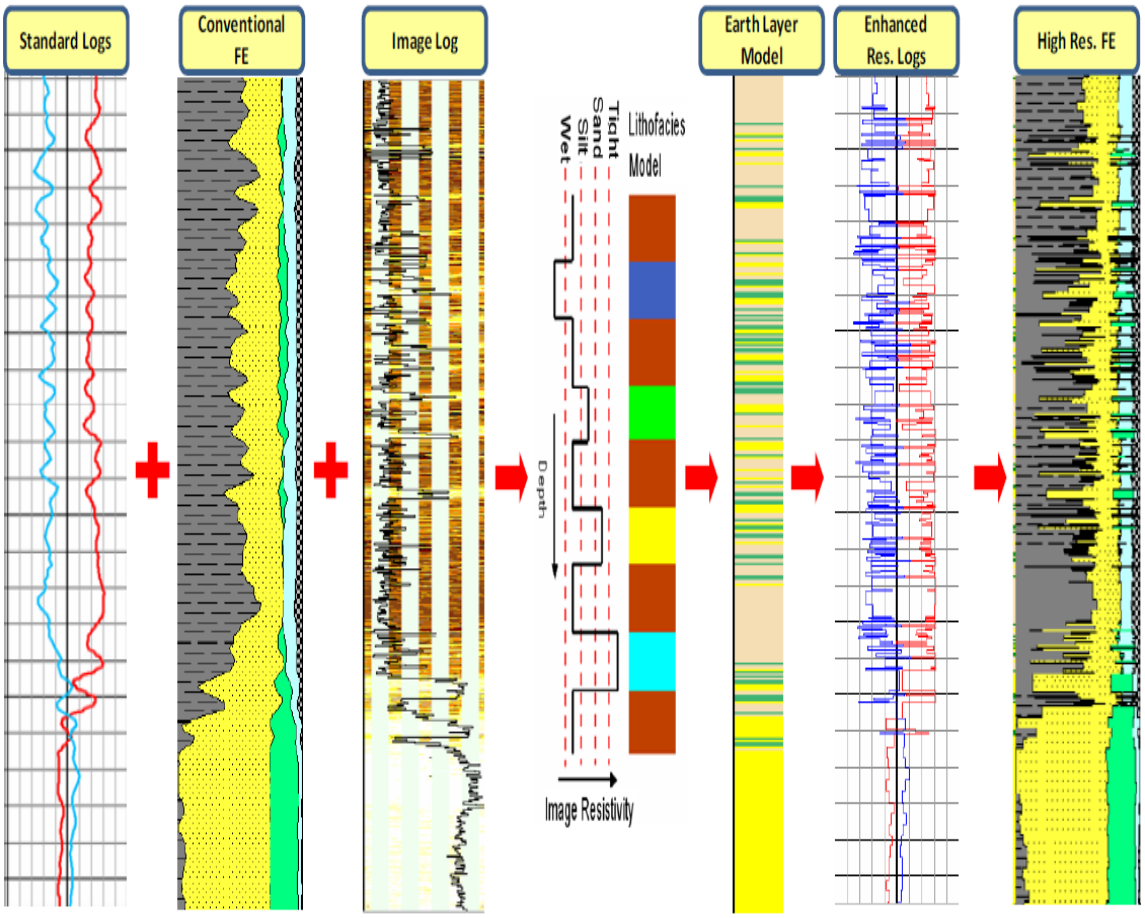

Figure 27.lithofacies descriptions from SRES cutoffs.(Daungkaew,S., et al 2008)

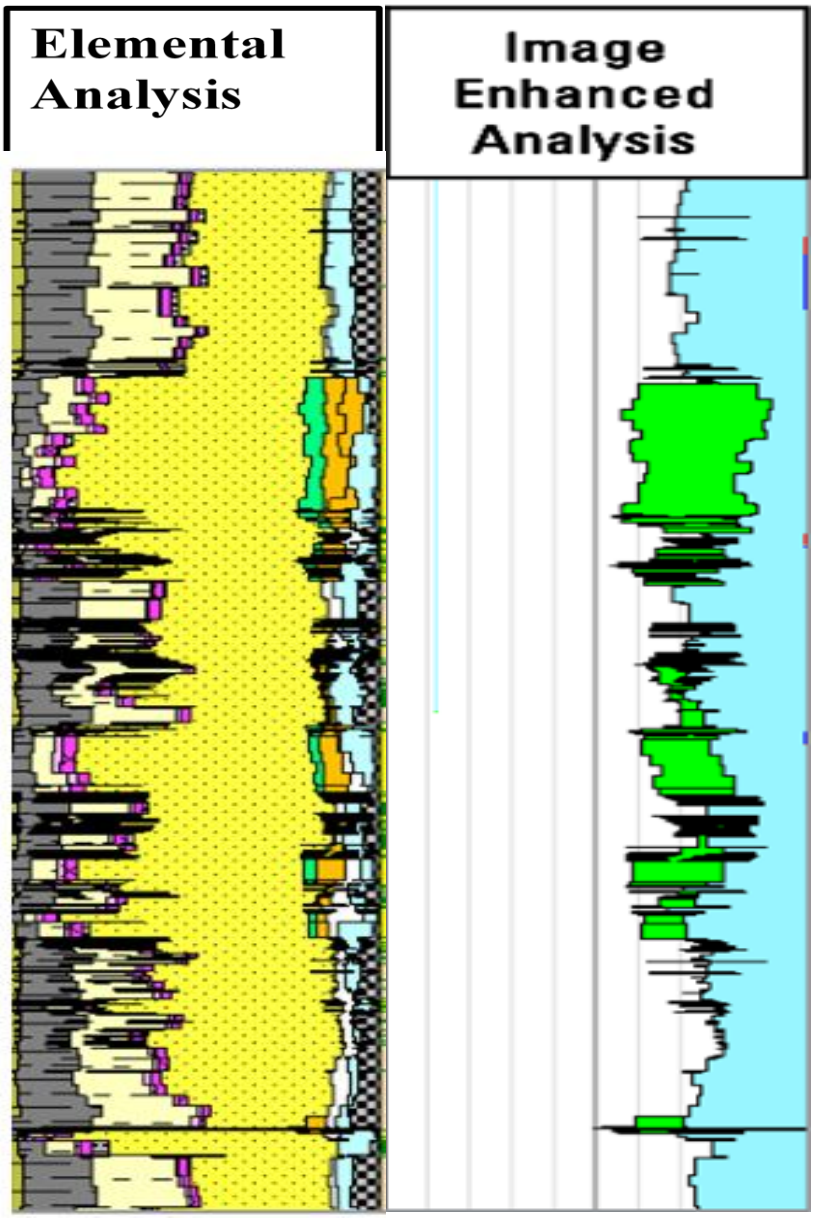

Figure 28.Track 1 shows the high resolution formation evaluation that is computed from the squared logs, and the corresponding fluid volume, as shown in track2. (Claverie, M. et al 2006)

CHAPTER 4

Literature Review

4.1 Integrating Acoustic Images, Dipmeters and Core Data in Thinly Bedded Sand Reservoirs

Lawrence, D. (SPWLA 2002) presented a comparison between acoustic image logs, UV core data and petrophysical Volume of Clay VCL analysis in order to compute NTG (net to gross) ratio among these three methods. The petrophysical analysis was implemented using various VCL cut-offs (30%, 40%, 50% and 60%). This comparison was applied in a number of wells of the following geological setting, Figure 29:

- Channel-levee deposits including the following facies: channel axis, channel margin, proximal and distal levee and splay deposits. Thin beds encountered in channel margins, levee settings and splay sands.
- Channelized lobe deposits with relatively high NTG (60-90%) descending towards lobe margins, where thin beds were well developed.

The UV core photos were depth-matched with acoustic images and X-ray scans were used to calculate Sand-Shale ratio. The acoustic images detailed hydrocarbon sand facies without considering cemented or clay matrix supported-muddy sands. The petrophysical VCL analysis was computed from Neutron-Density logs and calibrated with quantitative core measurements. Figure 30 and Figure 31 show the comparison results.

Generally, NTG calculated from the core and acoustic images show good match, although there is a slight overestimate in acoustic image net sands because it did not consider non-reservoir sand aspects (silts and cemented sands). The applied cut-offs in the VCL analyses were compared to NTG ratios from acoustic images. Certain facies associations were more sensitive to the applied cut-offs, like thinly-bedded layers (proximal levee and splay) while others such as massive sandstones (channel axis) were less sensitive. This means the VCL approach worked well only in relatively simple and thick-bed reservoirs.

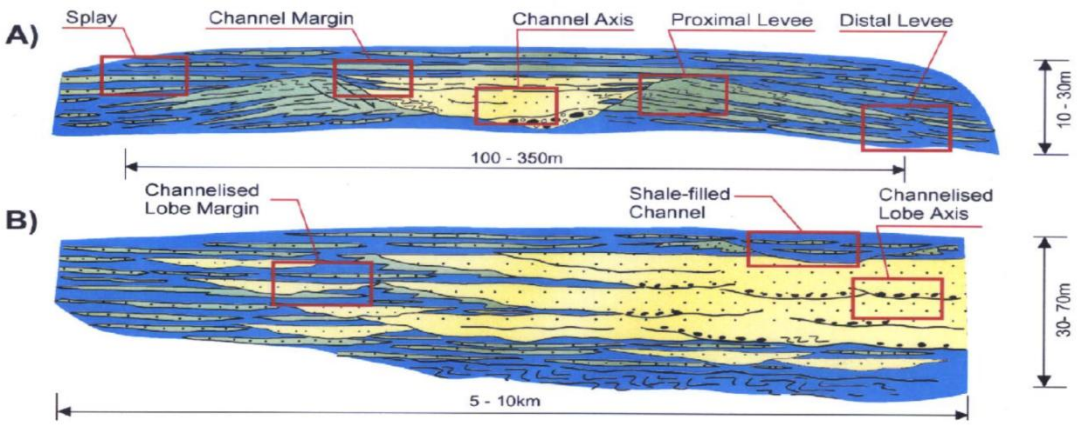

Figure 29.Depositional settings of the two-studied wells that are showing the distribution of thinly bedded sandstones (Lawrence, D., SPWLA 2002).

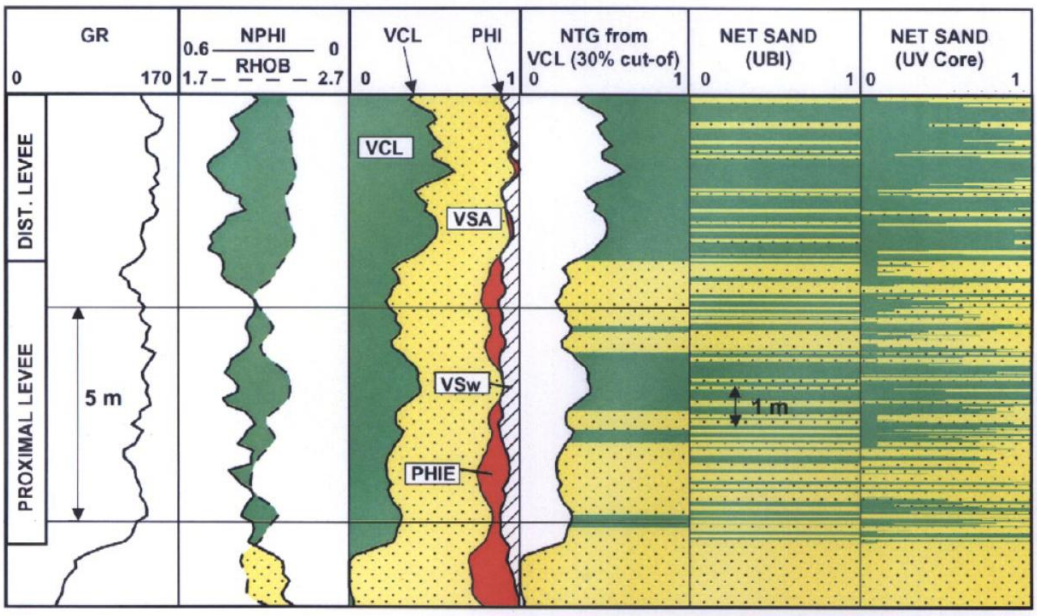

Figure 30.comparison of petrophysical VCL analysis, UV core data and acoustic image (Lawrence, D., SPWLA 2002).

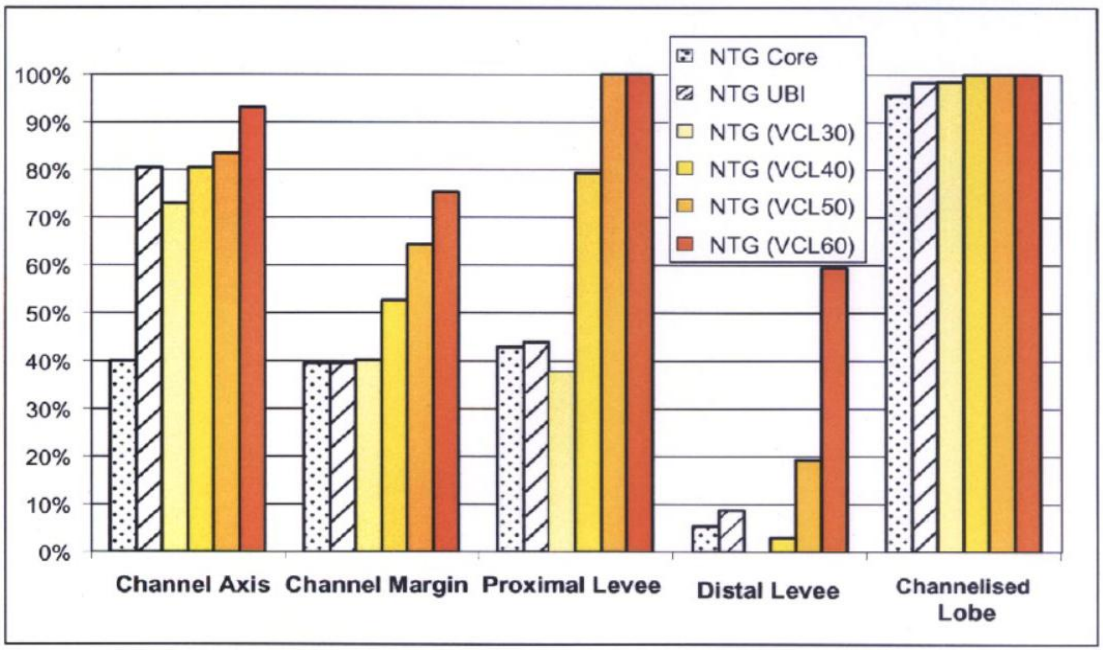

Figure 31.Comparison of NGT by facies association in well A between UV core data, acoustic images and VCL analysis (Lawrence, D., SPWLA 2002)

4.2 Thin sands evaluation using core data and Gamma Ray logs

Forsyth, D., et at. (1993) proposed an approach of evaluating the volume of laminated shale-sand sequence and resistivities attributed to the sand and shale layers in the lamination based on a parallel resistivity model.

Figure 32 shows the net sand count (white shading) and shale count (black shading) by deriving COR_Lam and Log_Lam from COR_Vsh and Log_Vsh respectively. These derivations were calculated by subdividing each 10 cm depth interval in proportion to the shale volume. Log_Vsh was computed from three different shale Gamma-ray values (100,110,120 API) with the same sand Gamma-ray (20 API). Log_Net represents the net sand reservoir using the 50% shale volume cut-off. The authors observed that COR_Lam and Log_Lam were more realistic representation of net reservoir compared to log_NET. Thus, a formation model was built based on the Log_Lam .A modelled laterlog deep resistivity curve was created from a forward modeling program and compared against the measured lateralog deep resistivity curve. Figure 33 shows the comparison using constant value of R_shale~3.6 Ω.m and four different modeled sand resistivity values (R_sand~5,7,10,20 Ω.m). The best fit among the modeled four runs was obtained using Rsand ~10-20 Ω.m. This R_sand values were then input to Archie's equation to compute Hydrocarbon saturations.

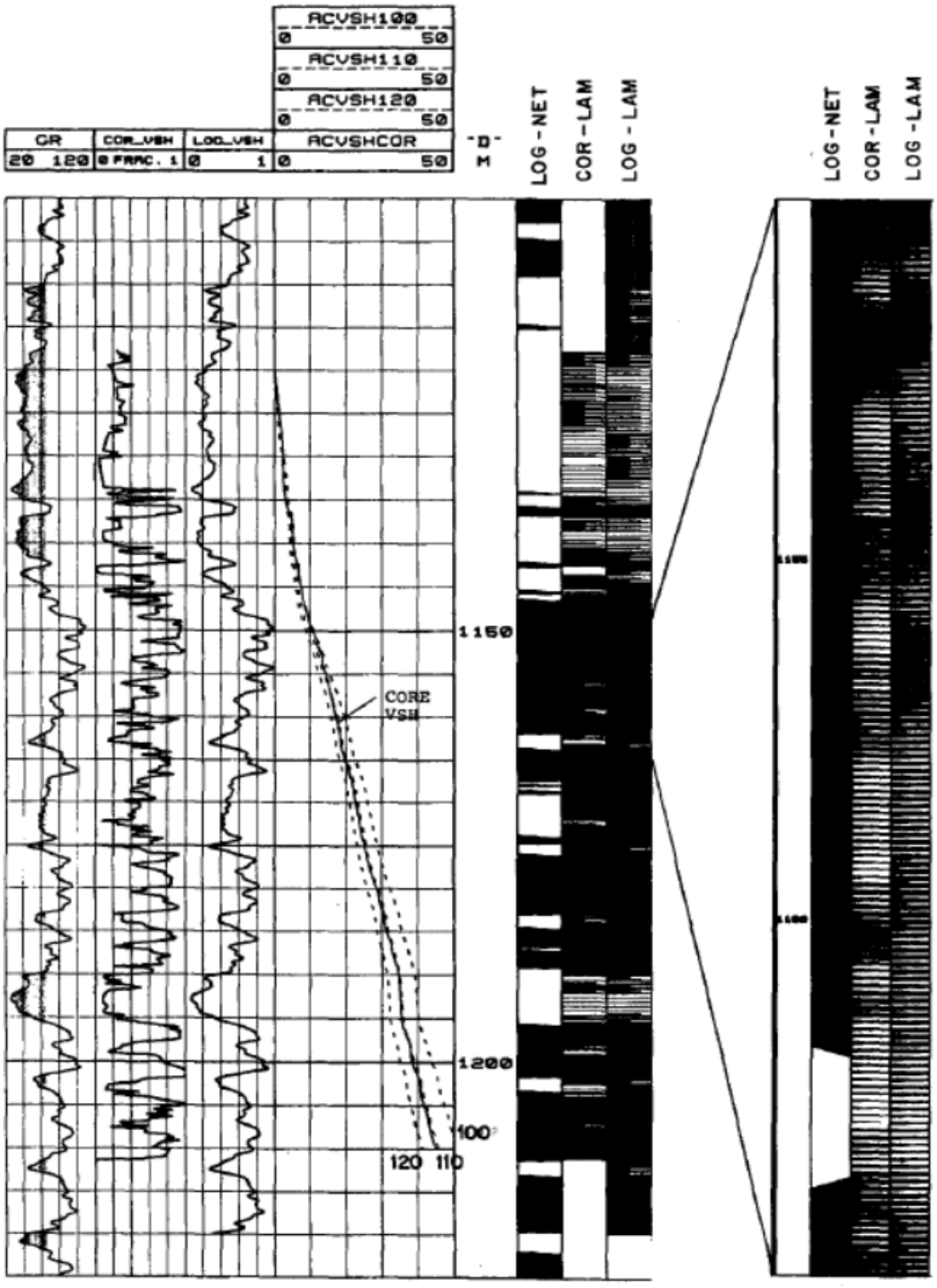

Figure 32.Computing COR_VSH and Log_VSH, and the corresponding COR_LAM and Log_LAM, compared to Lg_NET (Forsyth et at. 1993).

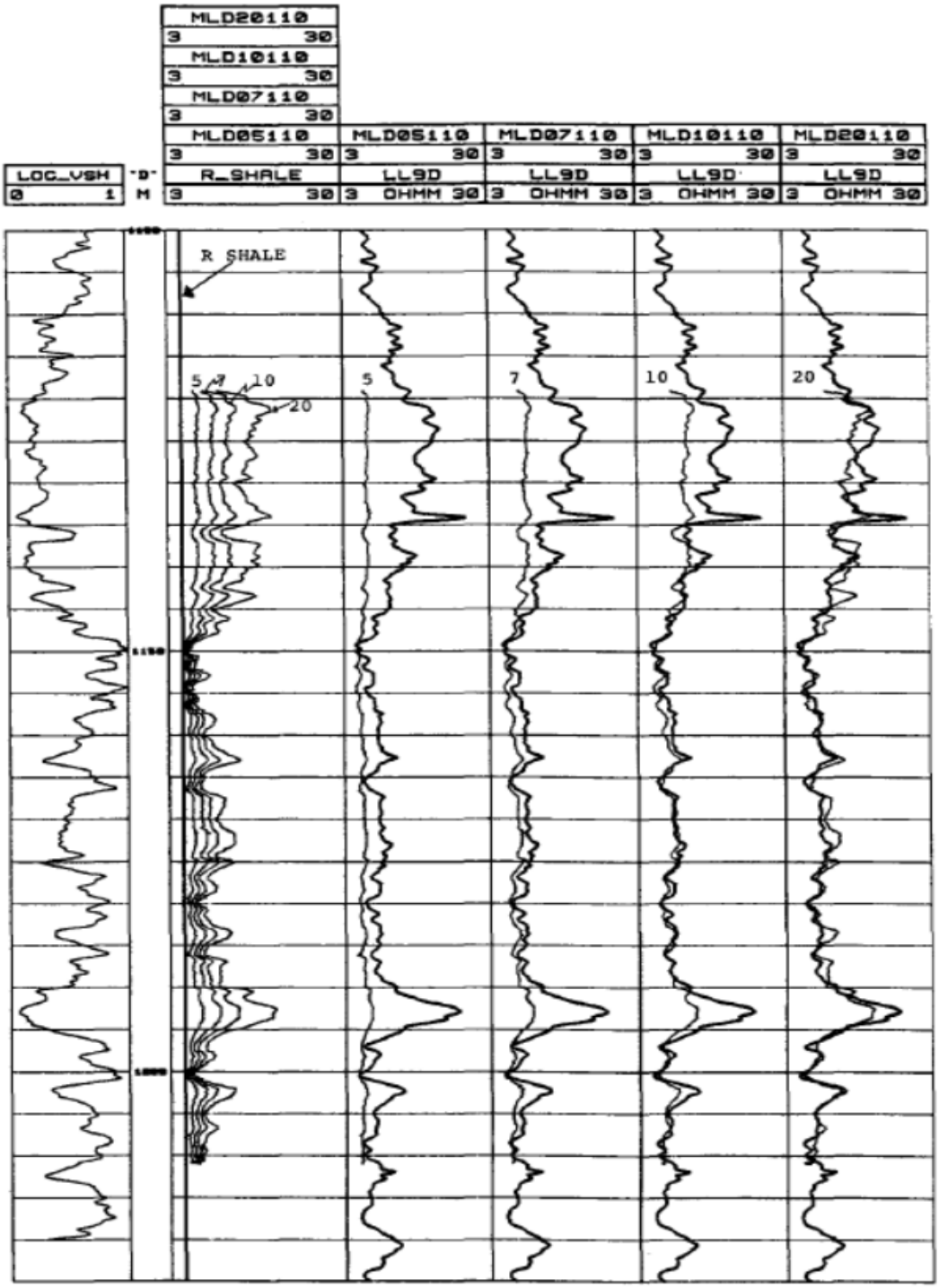

Figure 33.Modeled lateralog resistivity , using R_shale~3.6 Ω.m and R_sand~5,7,10,20 Ω.m, vs. measured one (Forsyth et at. 1993).

4.3 Graphical Analysis in Laminated Sand-Shale formation

Minh, C., et al (2007) established a graphical approach for evaluating laminated sand-shale sequence. This approach starts by plotting Rv vs. Rh in log-log plot. Then a user need to select the shale point where VCl is ~100%. Based on that, a butterfly overlay is created in terms of Rsand along the 45° line and Fsh increasing toward the west direction of the plot. After that, the user should suggest the lowest resistivity value in the 45° line to represent the wet resistivity value where water saturation is 100%, as shown in Figure 34.

The two values of Rshh and Rshv, that were determined based on the shale point selection, are used as inputs in Clavaud's equations to solve for Rsand, and hence, the accurate water saturation.

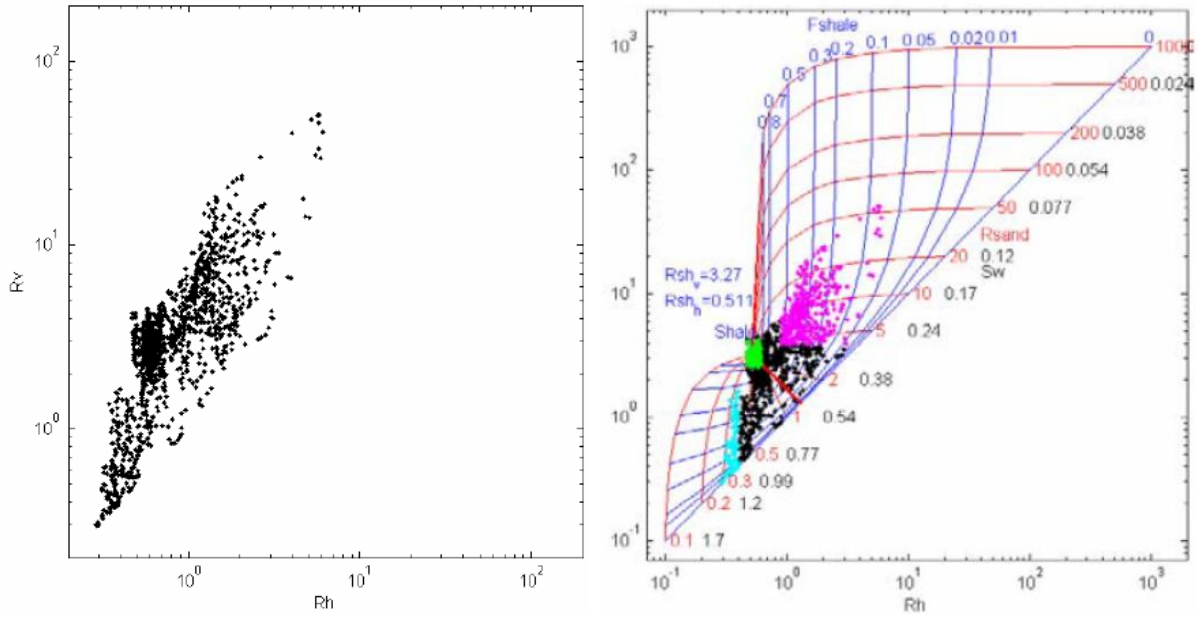

Figure 34.left: plotting measured Rv vs. Rh. Right: shale zone, water zones, and pay zones are shown in green, cyan and magenta, respectively (Minh, C., et al 2007).

CHAPTER 5

Case Studies

5.1 Well A

5.1.1 Background

The well in this study penetrated a number of formations. The formation of interest consists of complex fluvio deltaic sandstone system of Cretaceous age. It is composed mainly of Sandstone, siltstone, and shale interbeds. I used a comprehensive collection of open hole logs for the interpretation of this well. These are Density-Neutron-Gamma Ray,Wireline Nuclear Magnetic NMR, and a formation Image tool.

5.1.2 Laminated Sand-Shale analysis using Conventional Logs

Figure 35 shows the quick-look display of the conventional open hole logs that were acquired across the formation of interest (GR-Neutron-Density-shallow and deep Resistivity). The Neutron-Density scales are based on water-filled sandstone. It is obvious that the entire logged intervals (XX80-XX10 ft) exhibited shaly formations, due to relative high Gamma ray readings (~85 API), low resistivity values (<~10Ω.m) and relatively high separation between Neutron and Density curves. The neutron readings were high due to clay bound-waters (high Hydrogen-Index), and the high density of clay minerals confirmed the relatively high density readings. A sudden decrease in the Gamma rays was observed along the intervals (XX66-XX58 ft) and (XX20-XX10 ft)

with relatively high resistivity readings and less separation between neutron and density. The appearance of lithology looks changed in this interval from shaly into more coarse grains.

Based on these results, I performed a formation evaluation over these logged intervals using a Petrophysical Analysis Program to compute the mineralogy and the other petrophysical properties (porosity, VCL, saturation) as shown in Figure 36.

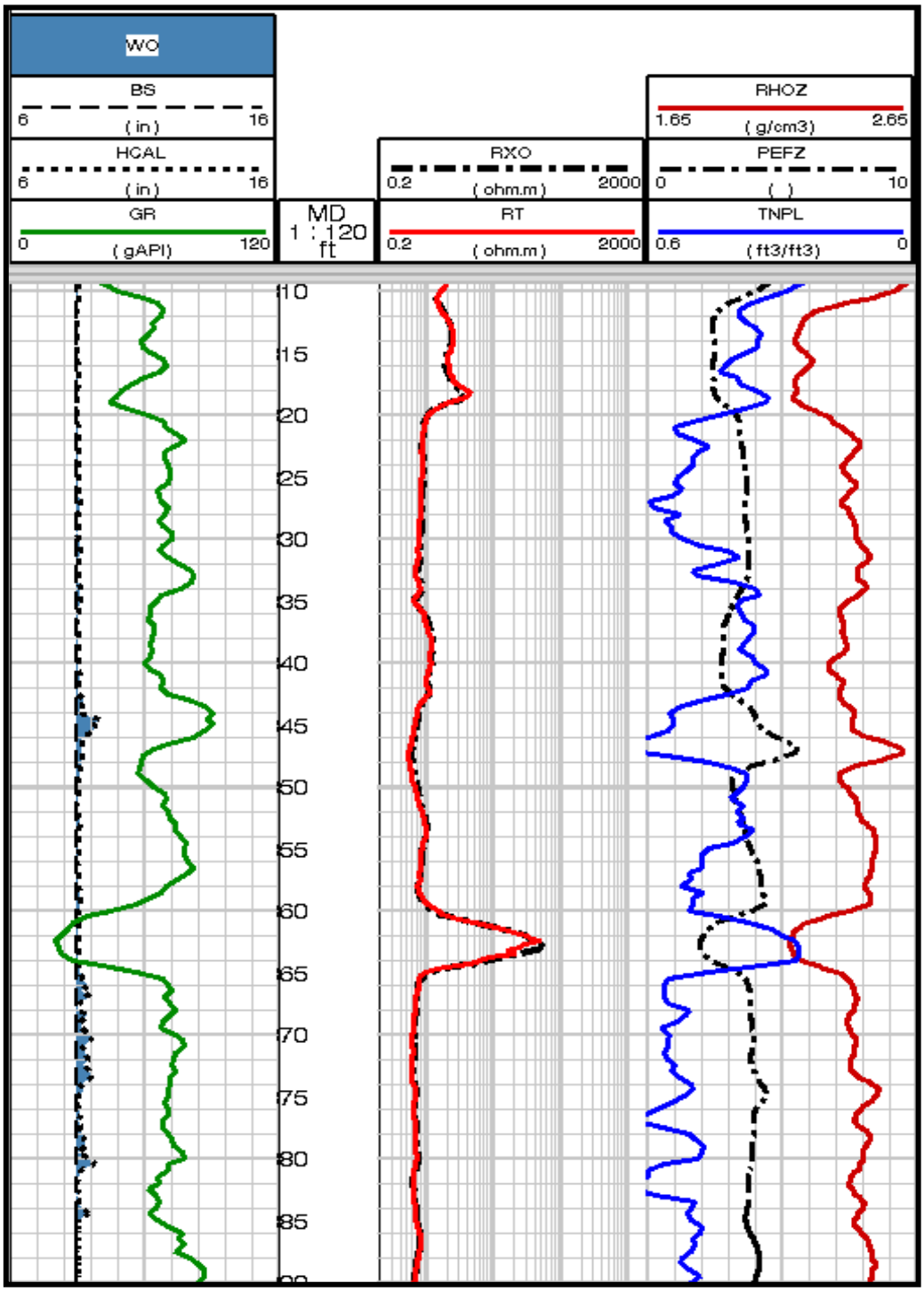

Figure 35.Conventional open hole logs. Track1: Gamma ray, caliper, BS, and washed-out zones (shading area) followed by depth track. Track2: Deep (Rt) and Shallow (Rxo) resistivity curves. Tack3: Neutron (TNPL), photoelectric (PEF) and density(RHOZ).

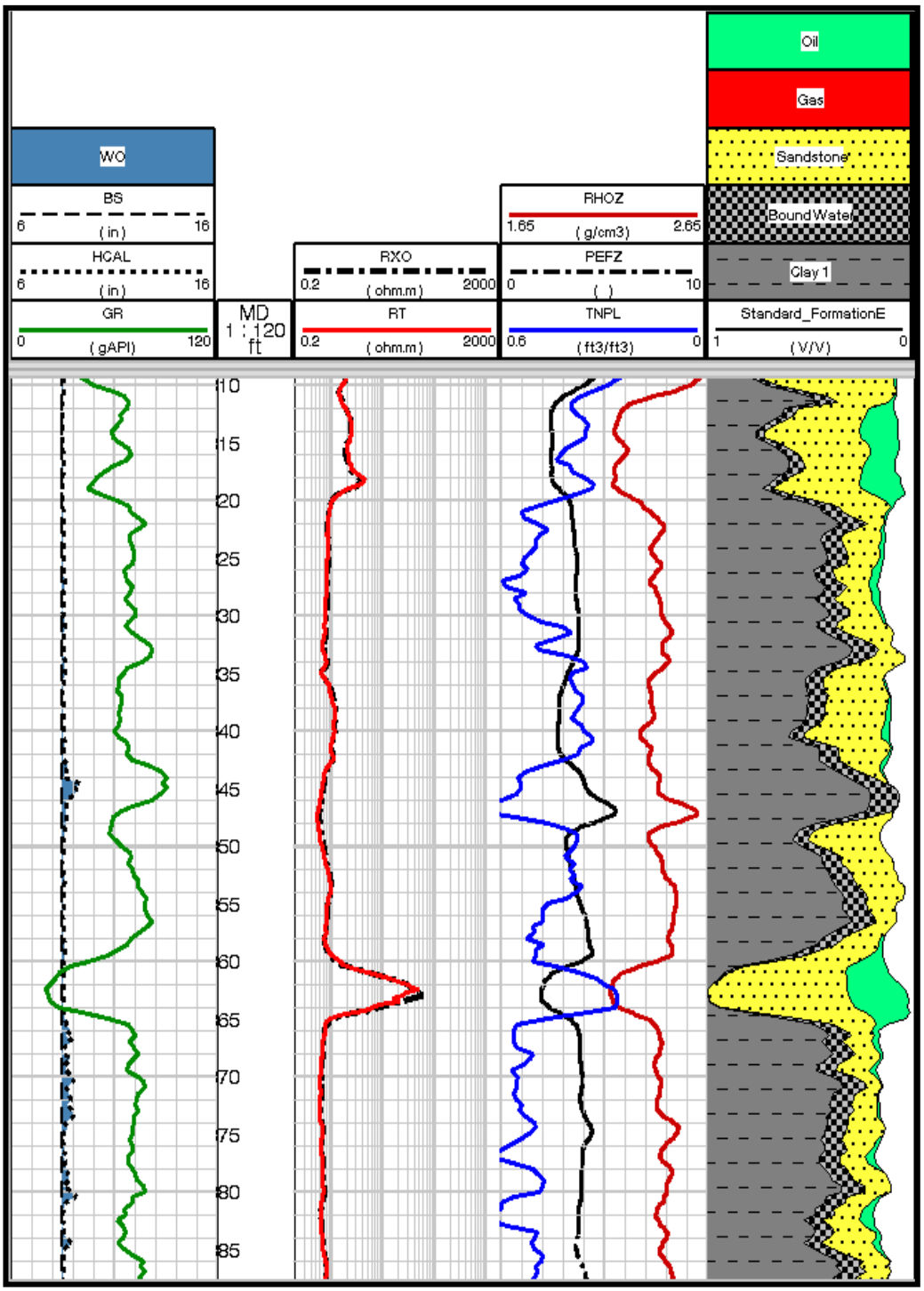

Figure 36.Track1: Gamma ray, caliper, BS, and washed-out zones (shading area) followed by depth track. Track2: Deep (Rt) and Shallow (Rxo) resistivity curves. Tack3: Neutron (TNPL), photoelectric (PEF) and density(RHOZ). Track4: Computed formation evaluation based only on the conventional logs.

The interpretation in Figure 36 indicates that there are two thick beds of hydrocarbon-filled sandstone at (XX66-XX58 ft) and (XX20-XX10 ft). The rest of the intervals are shaly-sand packages of high clay volume (averaging 65%) with very minor hydrocarbon volumes in the zone from XX40 ft to XX20 ft.

5.1.3 Laminated Shaly Sand Analysis adding NMR

Figure 37 shows my processed NMR analysis beside the previous results. The NMR results show that most of the T2 distributions are biased toward the low end of the spectrum indicating presence of small pores in the formation (shales), except the common intervals (XX66-XX58 ft) and (XX20-XX10 ft) where NMR results indicate porous intervals , as it was clear from the conventional analysis above. I found good agreement between NMR porosity with density porosity (DPHZ) and the neutron porosity (TNPH) as shown in track 3 in Figure 38. However, some of the T2 NMR distributions in the interval from XX55 ft to XX30 ft are biased towards the high end of the spectrum representing a producible zone that was hidden (underestimated) in the previous conventional formation evaluation.

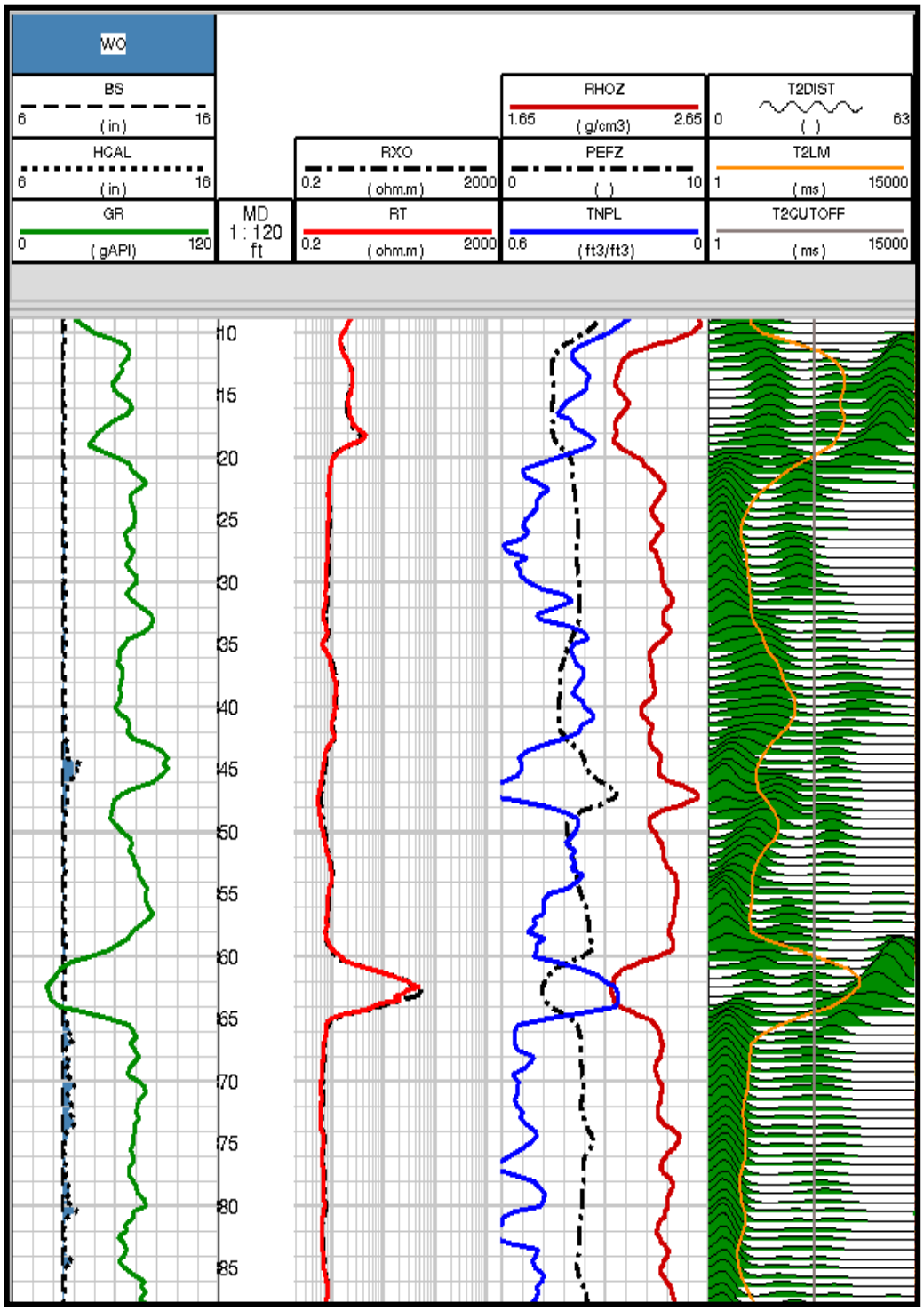

Figure 37.Track1: Gamma ray, caliper, BS, and washed-out zones (shaded area) followed by depth track. Track2: Deep (Rt) and Shallow (Rxo) resistivity curves. Tack3: Neutron (TNPL), photoelectric (PEF) and density(RHOZ). Track 4 shows the processed NMR analysis in terms of T2 distributions, T2cutoff and T2LM.

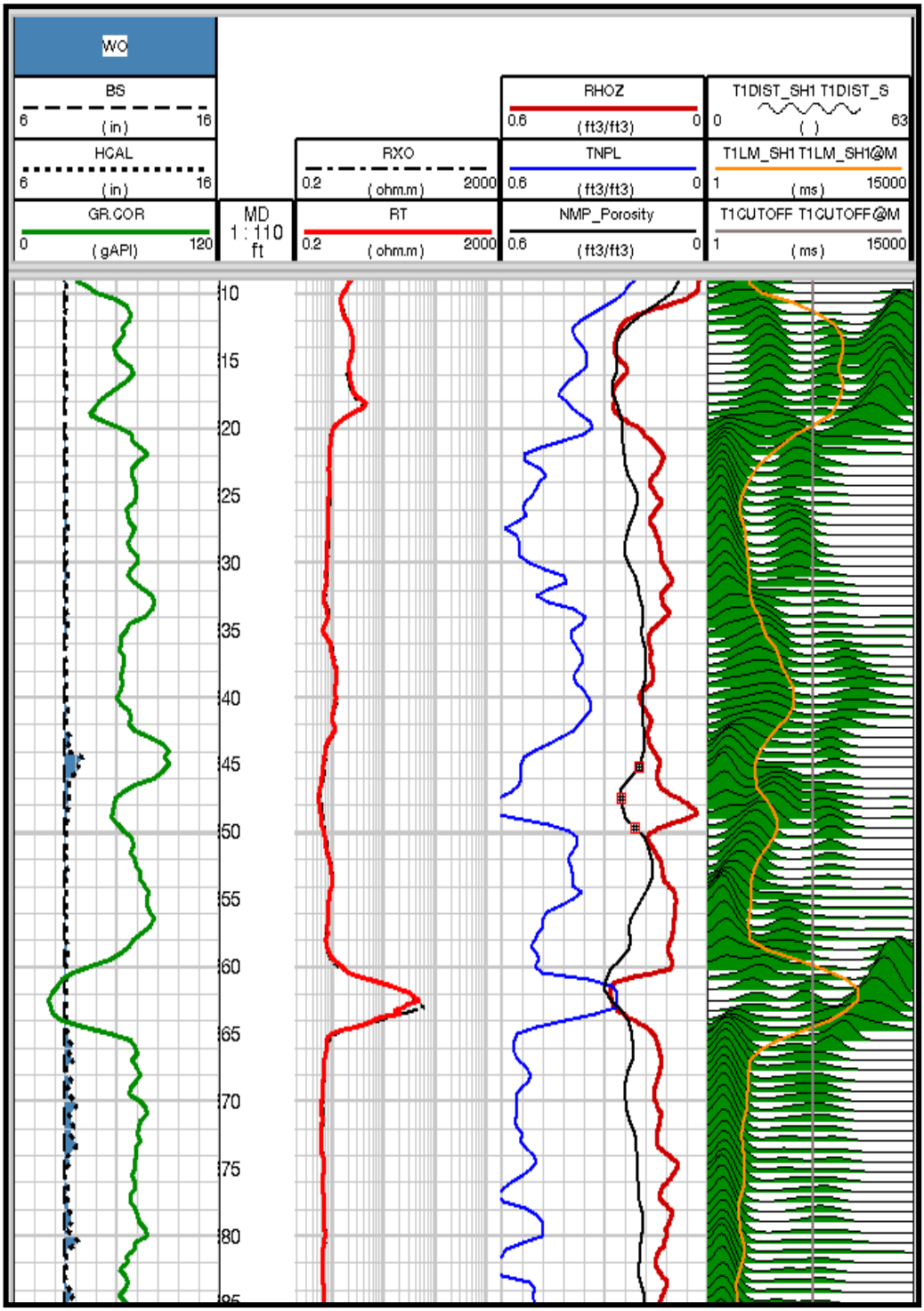

Figure 38.Track1: Gamma ray, caliper, BS, and washed-out zones (shaded area) followed by depth track. Track2: Deep (Rt) and Shallow (Rxo) resistivity curves. Tack3: Neutron (TNPL), density(RHOZ), and NMR total porosity. Track 4 shows the processed NMR analysis in terms of T2 distributions, T2cutoff and T2LM.

5.1.4 Laminated Shaly Sand Analysis Adding Borehole Images

I also processed a high-resolution borehole image in this formation. It is displayed beside the conventional logs and the NMR results, as shown in Figure 39. The thick beds at (XX66-XX58 ft) and (XX20-XX10 ft) are clearly shown in the image as resistive zones. There is clear evidence of lamination in the middle zone from XX55 ft to XX20 ft. The presence of some free fluids in that middle zone, as shown in NMR results, confirms that the formations suffer from thin bed problems, particularly in the zone from XX55 ft to XX20 ft.

Next, I performed SHARP processing utilizing the high resolution curve (SRES), in which a set of initial squared logs are created (RHOB, NPHI, GR, and RT). Figure 40 shows the optimized convolution results of this analysis. These high resolution squared logs were then imported into the same petrophysical interpretation program, which I had already used for the formation evaluation in the conventional analysis, to re-compute the formation evaluation as shown in Figure 41.

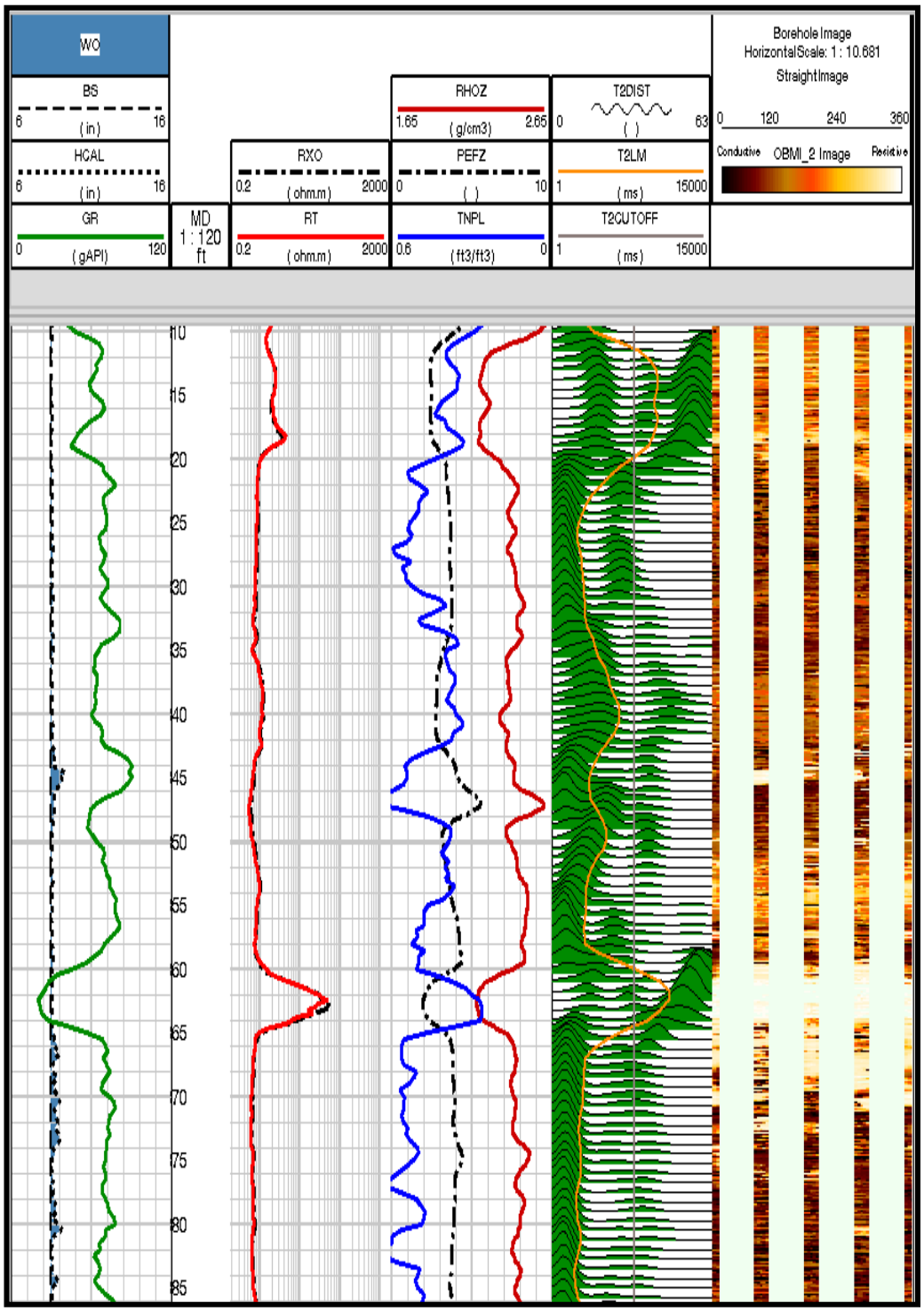

Figure 39.Track1: Gamma ray, caliper, BS, and washed-out zones (shaded area) followed by depth track. Track2: Deep (Rt) and Shallow (Rxo) resistivity curves. Tack3: Neutron (TNPL), photoelectric (PEF) and density (RHOZ). Track 4 shows the processed NMR. Track5: processed image logs.

The details in Figure 40 are as follows:

- The Depth track: measured depth.
- Track 1: Gamma Ray, comparison of the squared log after the optimization (red) and the convolution of squared log derived from optimization (green) and the original standard resolution log curve (black).
- Track 2: Lithofacies derived from SRES.
- Track 3: Borehole Image.
- Track 4: Resistivity, comparison of the squared log after the optimization (red) and the convolution of squared logs derived from optimization (green) and the original standard resolution log curve (black).
- Track 5: Density and Neutron, squared log curves after the optimization (blue and red).
- Track 6: Density and Neutron, the convolution of the squared logs derived from optimization (green) and original log curves (blue-TNPH, black-RHOB).
- Track 7: U (photoelectric volume), comparison of the squared log after the optimization (red) and the convolution of the squared log derived from optimization (green) and the original standard resolution log curve (black).

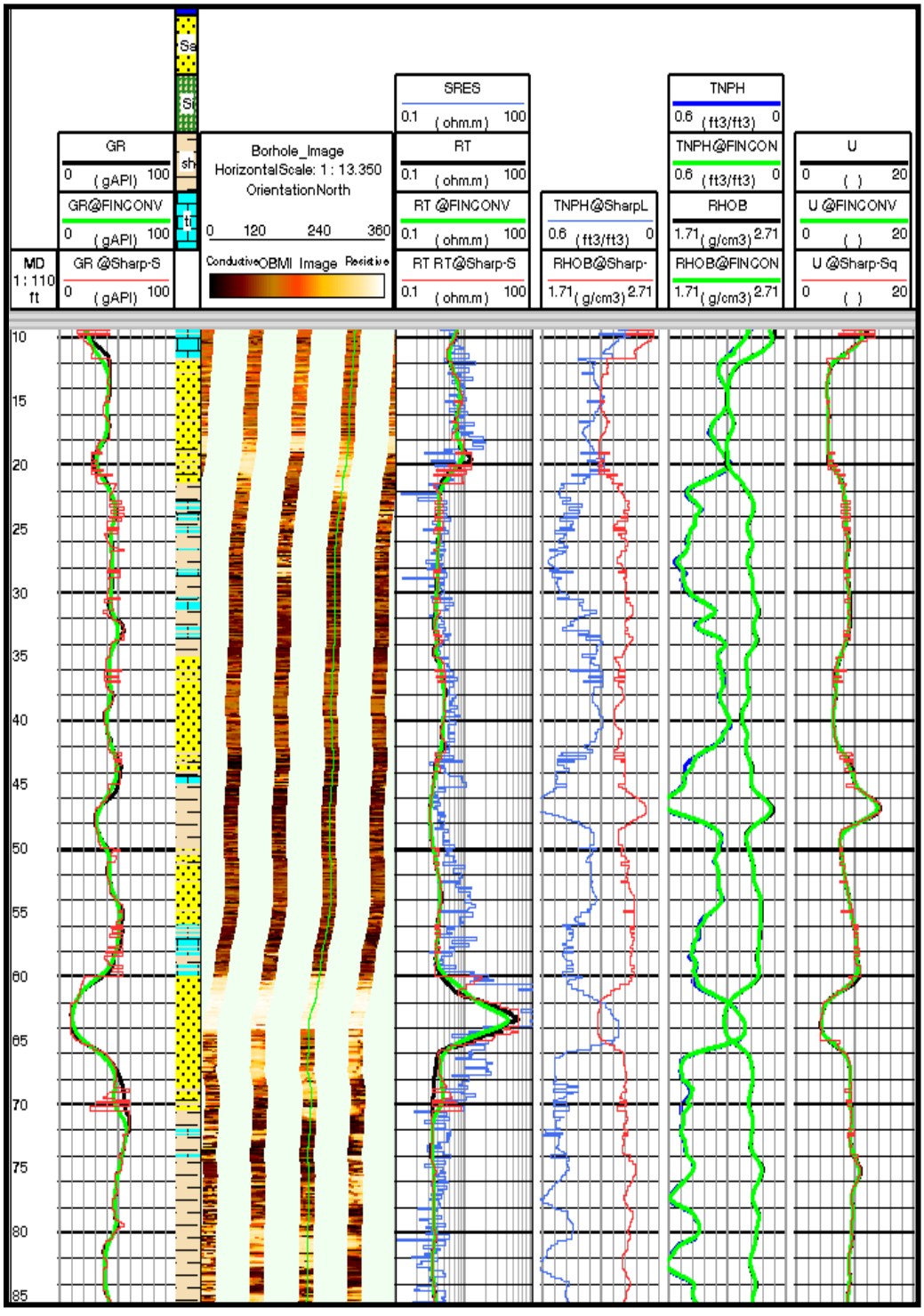

Figure 40.The deconvolution processing of the open hole logs using Sharp analysis.

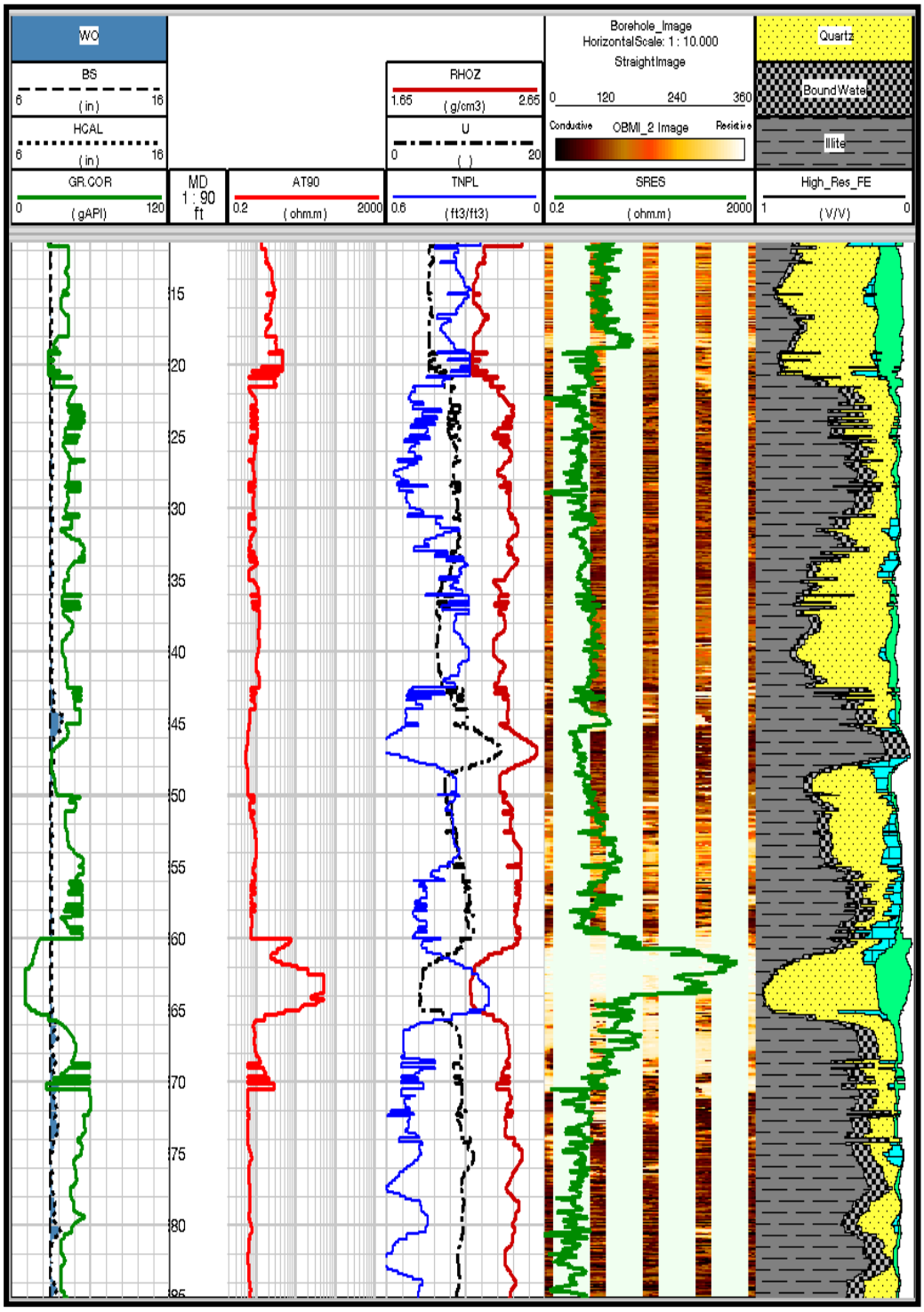

Figure 41.Track1: squared Gamma ray, caliper, BS, and washed-out zones (shaded area) followed by depth track. Track2: squared Deep (Rt) resistivity curve. Tack3: squared Neutron (TNPL), photoelectric (PEF) and density(RHOZ). Track 4. Borhole image along with SRES. Track5: high resolution formation evaluation.

5.1.5 Discussion

The thick beds in the intervals (XX66-XX58 ft) and (XX20-XX10 ft) are clearly identified by the conventional analysis, but adding the NMR results and the borehole image into the analysis show additional hydrocarbon volumes exist in the middle zone (XX55 ft –XX30 ft) that was proved as thin bed zone. Generally, moving gradually from the standard evaluation (the conventional logs) to the high resolution evaluation, using the NMR and the deconvolution techniques from the image logs, shows improvement in hydrocarbon volumes, particularly in the interval from XX55 ft to XX30 ft as shown in Figure 42.

Table 1 shows numerical comparison in the thin bedded pay zone (XX55 ft –XX30 ft) between the conventional analysis and the high resolution analysis (NMR and borehole image)

	Conventional Analysis	**LSA (** NMR and borehole image)
<SUWI>	**0.89**	**0.68**
<VCL>	**0.65**	**0.45**

Table 1.Comparing total water saturation SUWI and clay volume VCL between conventional analysis and LSA in the interval (XX55ft-XX30ft).

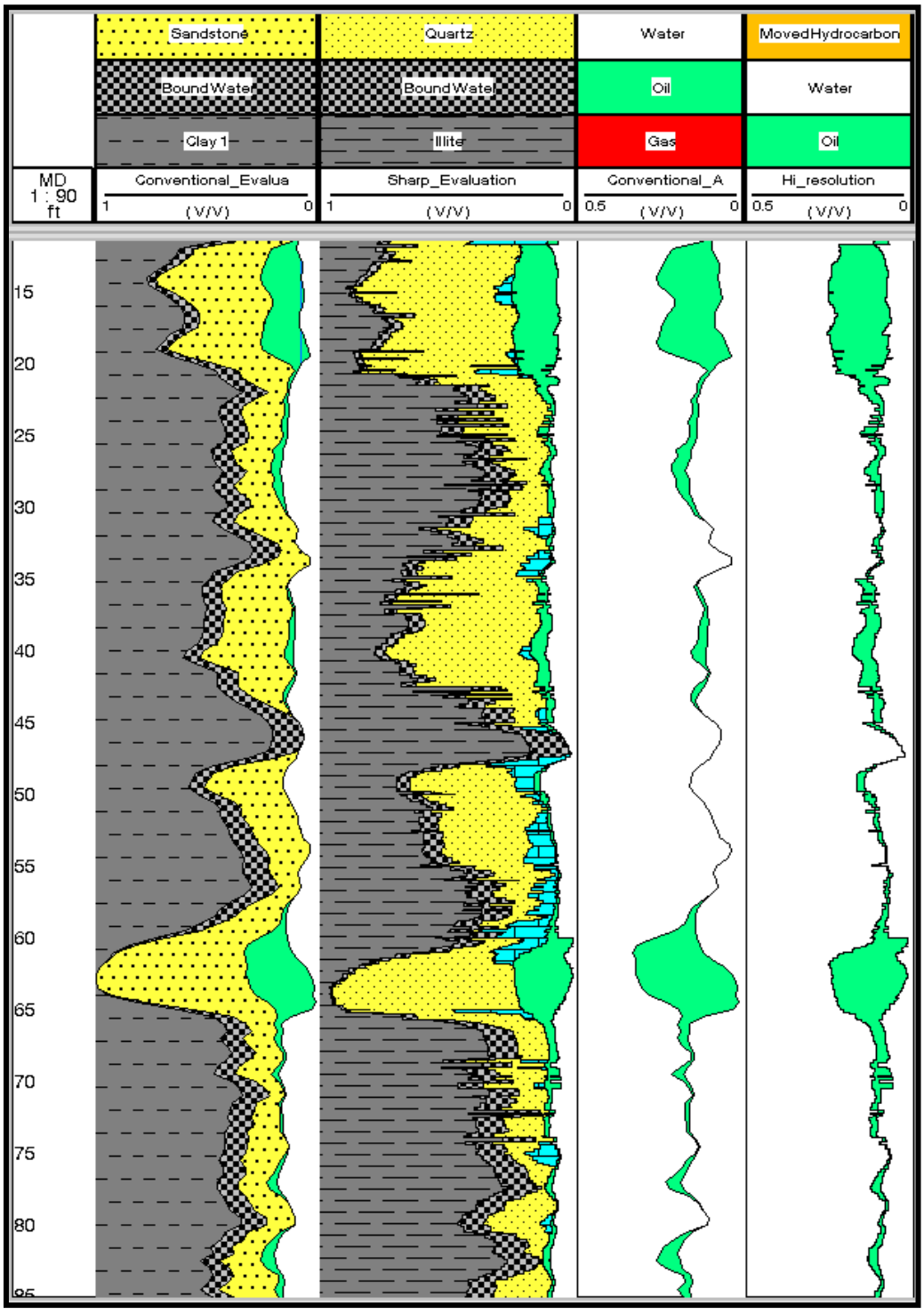

Figure 42.Comparing fluid volumes between conventional analysis and LSA.

5.2 Well B

5.2.1 Background

An offshore exploration well drilled across a siliciclastic reservoir with formations formed under turbiditic depositional environments. The sediments are mainly from middle Miocene and younger siliciclastic. The deposition occurred at the base of the continental slope and on the abyssal plain.

In addition to the conventional logs, I processed the wireline NMR and the Triaxial Resistivity Induction logs to show improvement in the hydrocarbon estimation along the laminated sand-shale intervals. In a later stage, I compared and validated all of these analyses to tested core labs.

5.2.2 Thin Bed Evaluation: Conventional logs and NMR

In this well, an array of resistivity logs were acquired, as shown in Track 2 of Figure 43, of different depth of investigations (R10”,R20”,R30”,R60”,R90”).

Quick analysis starting from the conventional logs in Figure 43, gives high impression of shaly-sand formations.

The intervals (XX550-XX480 ft) and (X250-X900 ft) have identical formation properties: relatively high gamma ray reading, low resistivity (~3 ohm-m) readings, all resistivity arrays are overlay (no invasion), and high separation between neutron-density curves. These two intervals should be clastic zones of very high clay volumes (shaliness). However, the interval from X450 to X250 ft has different properties compared to the top and bottom sections. I observed an abrupt drop in the Gamma ray readings, slight

increase in resistivity log readings (~10 ohm-m), and less separation between neutron-density curves. Therefore, this interval (X450-X250 ft) could be a potential pay zone.

The T2 distribution of the NMR logs, in Track 4 of Figure 44, is generally biased towards the high end of the spectrum in the interval from X450 ft to X250 ft, indicating the existing of relatively high porous zones filled with fluids. The same behavior of T2 distribution can be seen isolating intervals in the top section, for example the zone from X200-X150 ft.

I combined all these logs i.e. conventional logs and NMR, into a petrophysical interpretation program to compute the formation evaluation (mineralogy, porosity, V_{CL}, saturation) as shown in Figure 45.

The interpretation in Figure 45 reveals my analysis above, in which the interval from X450ft to X250 ft is indeed shaly-sand with hydrocarbon filling the sand grains.

I analyzed a Thomas-Stiber plot in terms of PHIT (total porosity) vs. volume fraction of shale (Vcl), Figure 46, along the interval X450-X250 ft. One can see that most of the data fell along the laminated line with minor amounts of dispersed shale indicating that the formation at that zone (X450-X250 ft) is candidate for laminated shaly-sand analysis.

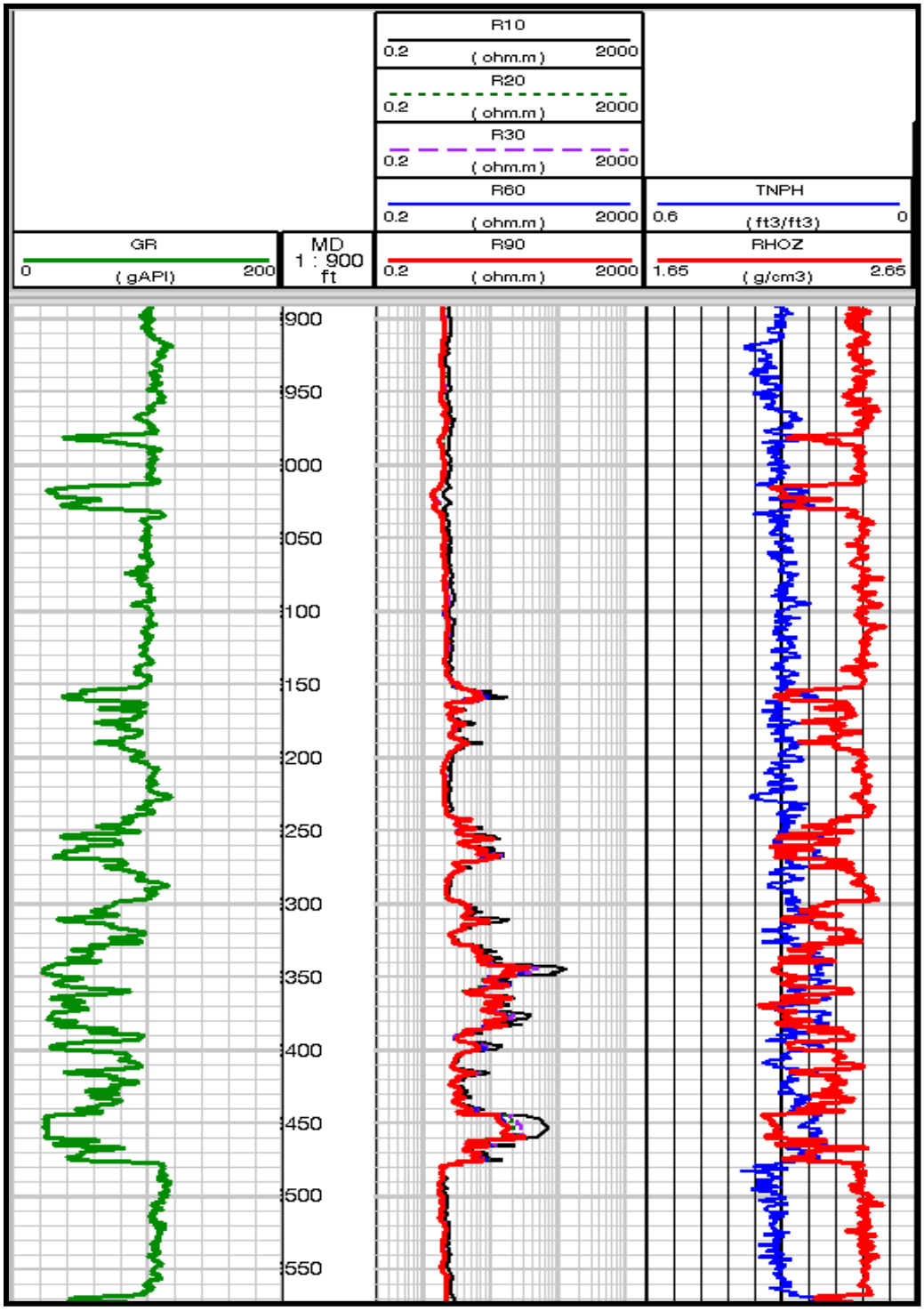

Figure 43.Conventional open hole logs. Track1: Gamma ray, followed by depth track. Track2: five array resistivity logs. Tack3: Neutron (TNPH), and density(RHOZ).

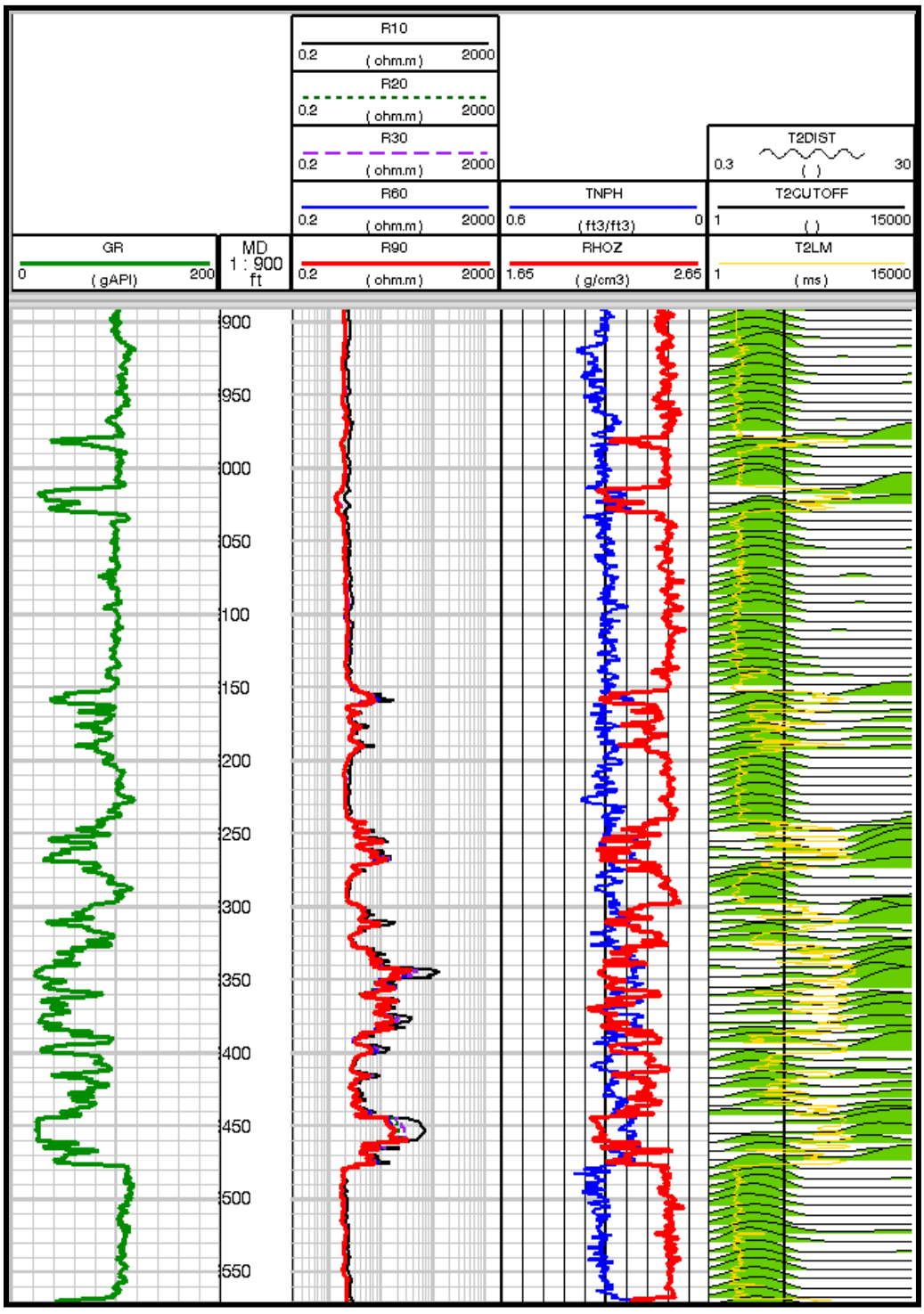

Figure 44.Track1: Gamma ray, followed by depth track. Track2: five array resistivity logs. Tack3: Neutron (TNPH), and density(RHOZ). Track4: processed NMR in terms of T2 distribution, T2cutoff and T2LM.

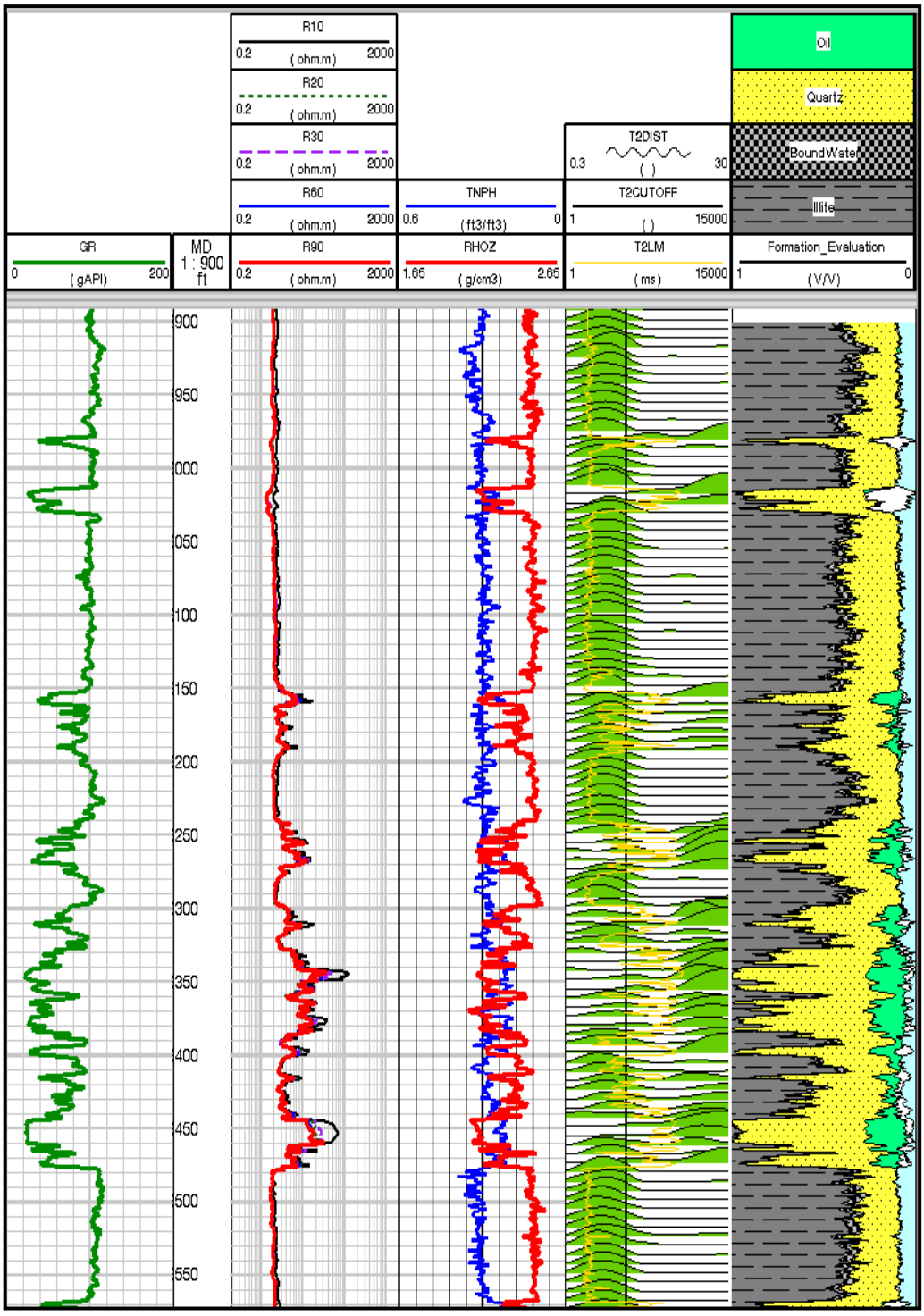

Figure 45.Track1: Gamma ray, followed by depth track. Track2: resistivity logs. Tack3: Neutron (TNPH), and density(RHOZ). Track4: processed NMR. Track5: computed formation evaluation.

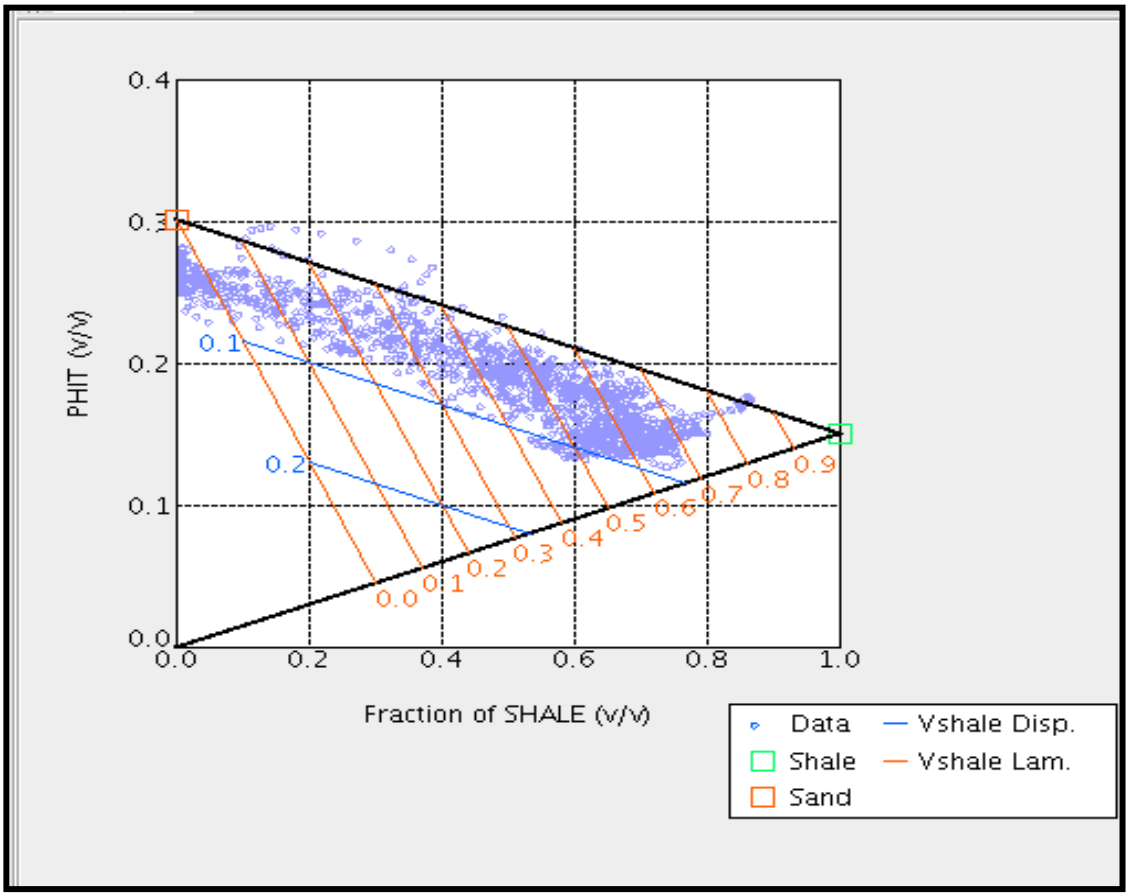

Figure 46.Thomas-Stieber plot along the interval XX450-XX250 ft.

5.2.3 Thin Bed Evaluation: Triaxial Resistivity logs (Resistivity anisotropy)

I applied the 1D-inversion algorithm on the Triaxial resistivity logs and generated the R_V and R_h logs as shown in Figure 47. As can be seen, the resistivity anisotropy is varying along the whole interval, but it is the highest in the thin-bedded pay zone (X450-X250 ft). The anisotropy is around 2-3 in the shale sections at the top and bottom of the thin-bedded pay zone (X450-X250 ft), as shown in Figure 48. Therefore, I used the shale anisotropy factor α=2.5 as input for the laminated sand-shale analysis in this well.

Applying the workflow described in section 3.4, I computed the following outputs: R_{sand}, F_{sand}, and R_{shh}. Since $R_h > R_{h\_lim}$ (as it is obvious from track2 in Figure 49), I computed R_{sand} and R_{shale} from these equations:

$$R_{shh} = \frac{R_v - R_h * (1 - F_{sh\_lam})^2 + \alpha * R_h * F_{sh\_lam}^2 - \sqrt{[R_v + R_h * (F_{sh_{lam}} * (1 - \alpha) - 2) + 1)]^2 - 4 * (1 - F_{sh_{lam}})^2 * R_h * R_v}}{2 * \alpha * F_{sh\_lam}}$$

$$R_{sand} = \frac{R_v + R_h * (1 - F_{sh_{lam}})^2 - \alpha * R_h * F_{sh_{lam}}^2 + \sqrt{[R_v + R_h * (F_{sh_{lam}} * (1 - \alpha) - 2) + 1)]^2 - 4 * (1 - F_{sh_{lam}})^2 * R_h * R_v}}{2 * \alpha * F_{sh_{lam}}}$$

Then, I used these values then as inputs for computing water saturation in shales (Sw_shale),in sands(Sw_sand), and total water saturation (Swt). These results are illustrated in Figure 50.

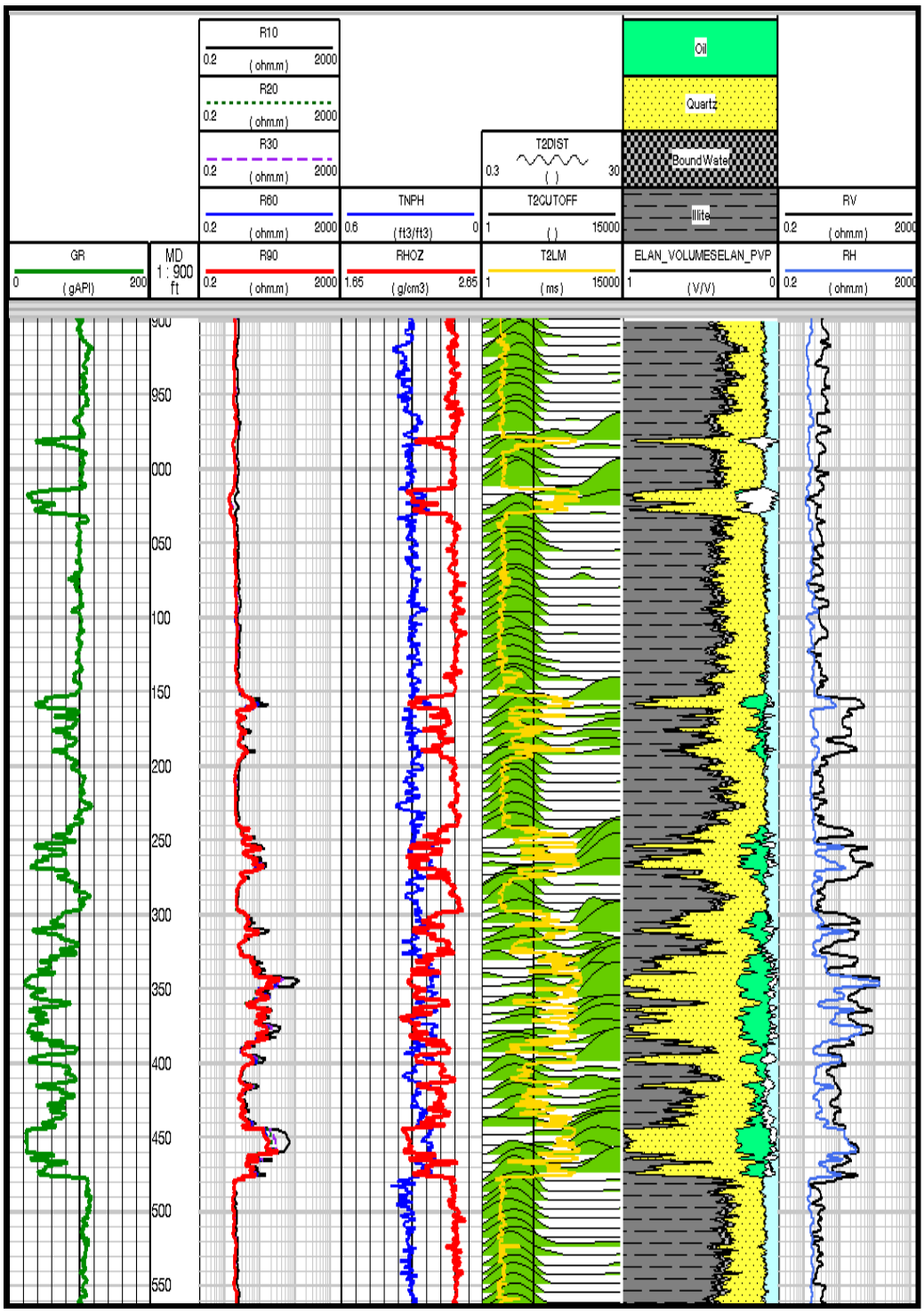

Figure 47.Track1: Gamma ray, followed by depth track. Track2: resistivity logs. Tack3: Neutron (TNPH), and density(RHOZ). Track4: processed NMR. Track5: computed formation evaluation. Track6: inverted vertical resistivity (Rv) and horizontal resistivity (RH).

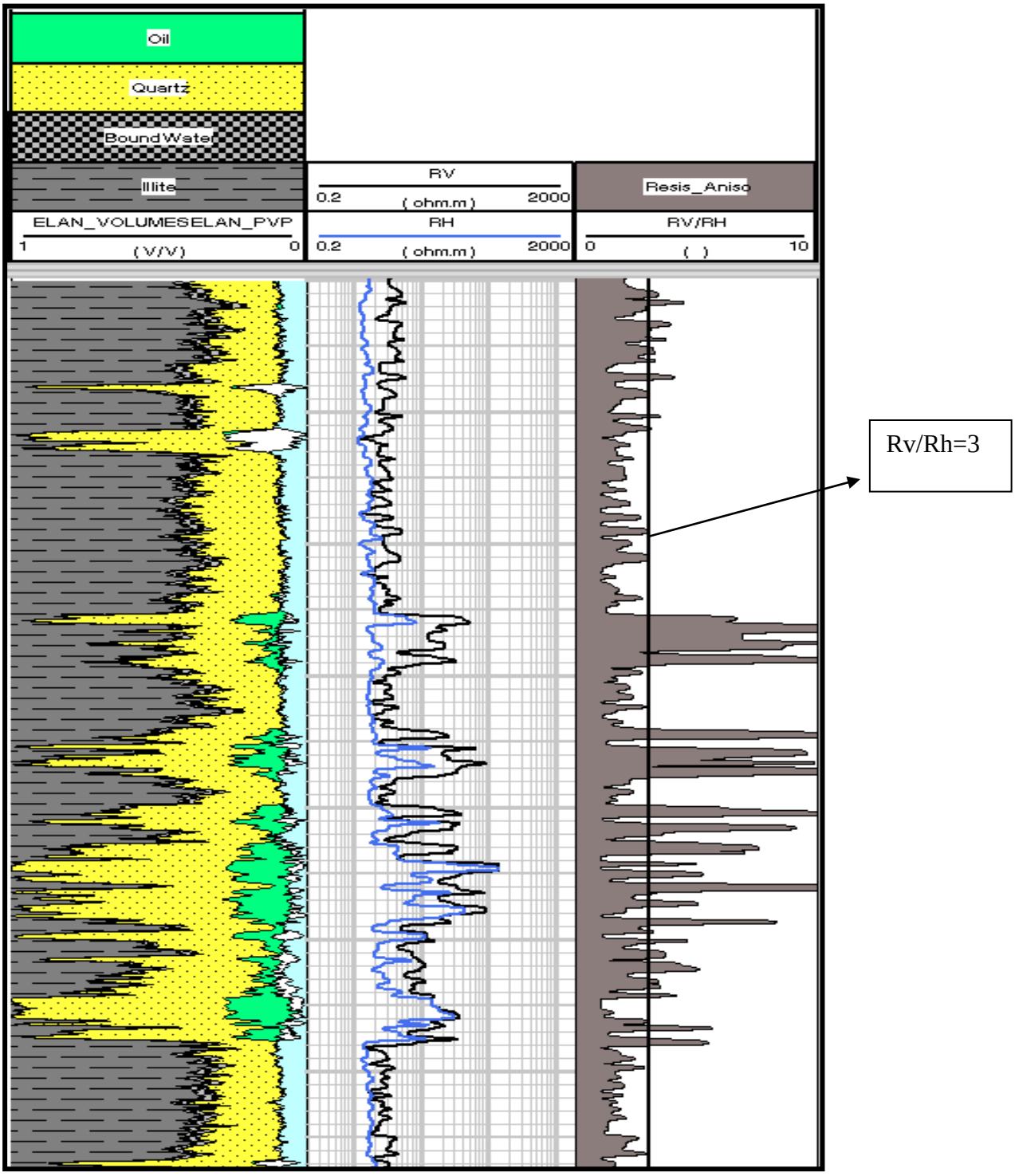

Figure 48.Track1: computed formation evaluation. Track2: Rv &RH. Track3: RV/RH, and constant ratio displayed by the constant line at Rv/Rh=3.

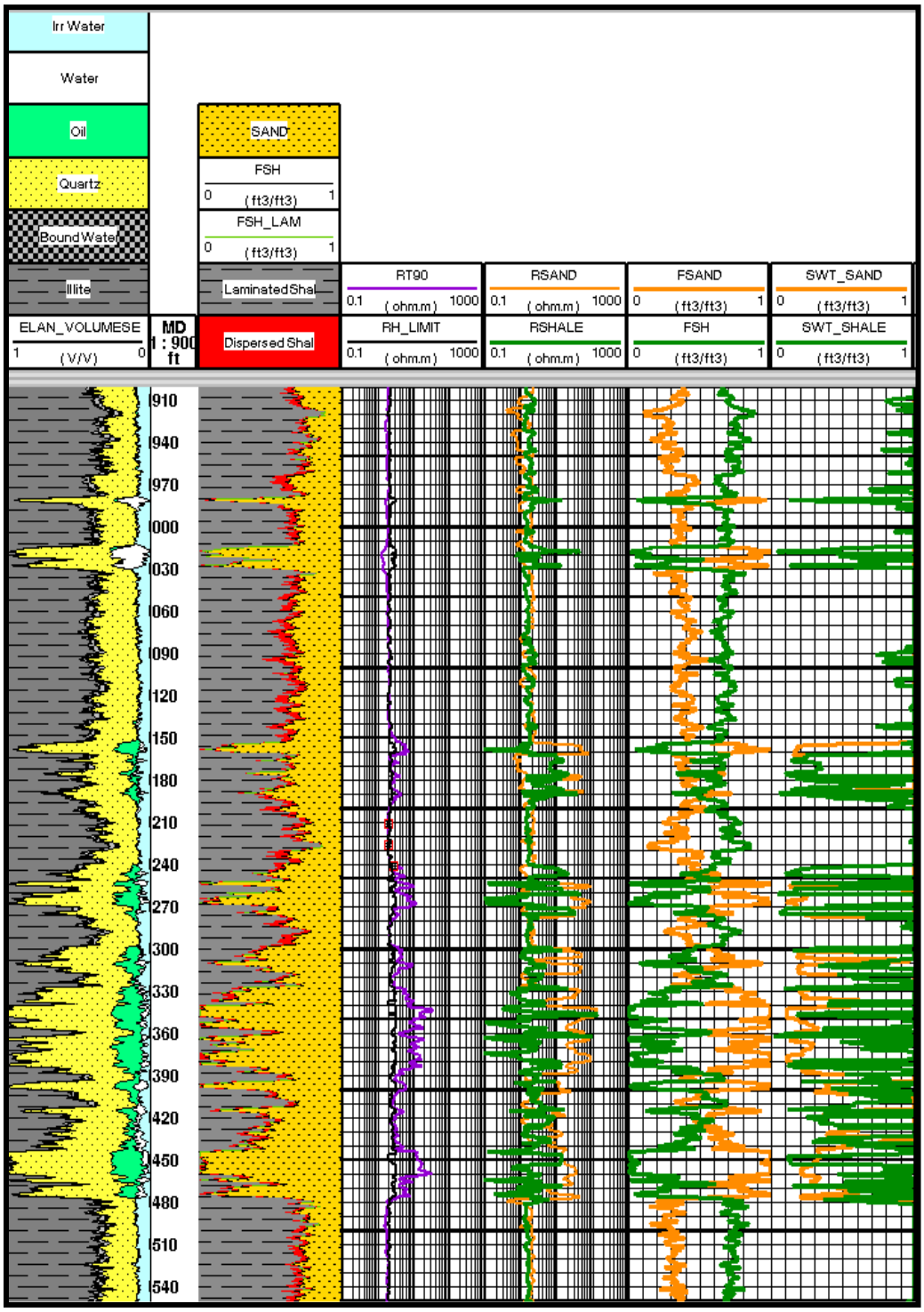

Figure 49.Track1: computed formation evaluation followed by depth track. Track2: laminated volume vs. dispersed volume in the sand grains. Tack3: computed RH_Limit and Rt90=RH. Track4: computed resistivity in the sand particles (RSAND) and in the shale particles (RSHALE). Track5: fraction volume of the sand (FSAND) and of the shale (FSH). Track6: computed water saturation in the sand (SWT_SAND) and in the shale (SWT_SHALE).

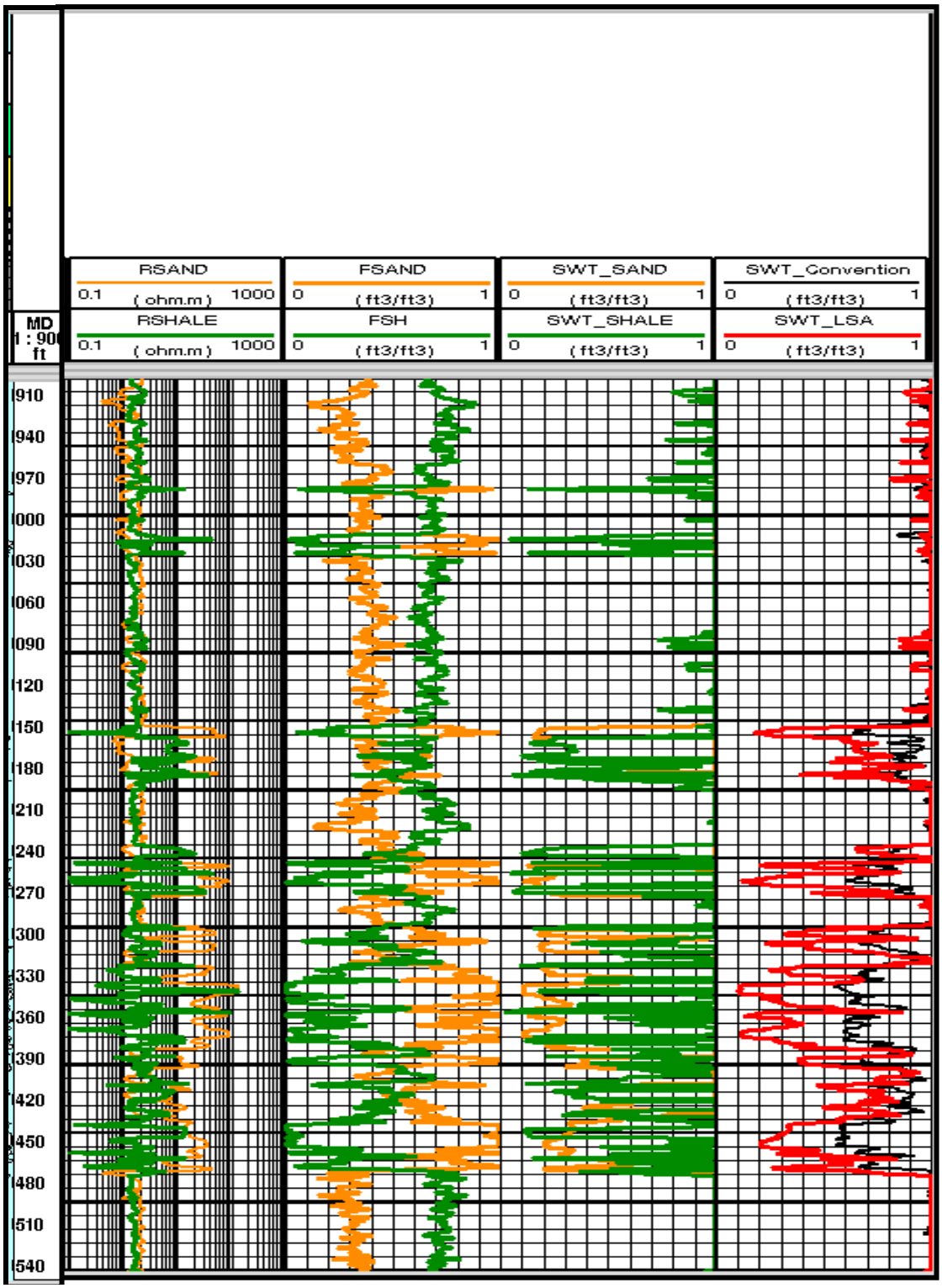

Figure 50..Depth Track. Track1: computed resistivity in the sand particles (RSAND) and in the shale particles (RSHALE). Track2: fraction volume of the sand (FSAND) and of the shale (FSH). Tack3: computed water saturation in the sand (SWT_SAND) and in the shale (SWT_SHALE). Track4: computed total water saturation from LSA Rv & RH using α=2.5 (SWT_LSA) and conventional total water saturation from only RH.

5.2.4 Discussion

The wireline NMR was helpful in identifying hydrocarbons in the thin bedded pay zone (X450-X250 ft) by separating free fluid and bound fluid volumes applying 0.3 msec cutoff values. However, adding the Triaxial induction measurements unlocked those "not-so-obvious" intervals in the thin bedded pay zones. Figure 50 shows the improvement in the hydrocarbon estimations in terms of the computed total water saturation SWT_LSA utilizing the analysis from Rv and RH simultaneously instead of using only RH as in the conventional analysis SWT_Conventional. Table 2 summarizes these results.

The shale anisotropy (α) plays a critical role in estimating the resistivity of each component (sand/shale) in the model. To emphasize this point, I recomputed Swt by ignoring the shale anisotropy (i.e. taking α=1) and compared the results to the previous computation of Swt when I used α=2.5. No difference can be seen in the thin bedded pay zone (X450-X150 ft), while the top and bottom shale sections show erroneous hydrocarbon saturations, which do not make sense in zones of such high shale content, as shown in Figure 51.

	Conventional Analysis (Rh only)	**LSA (Rv & Rh)**
<SWUI>	**0.78**	**0.63**

Table 2. Comparing total water saturation SUWI between conventional analysis and LSA in the interval (X450-X250 ft).

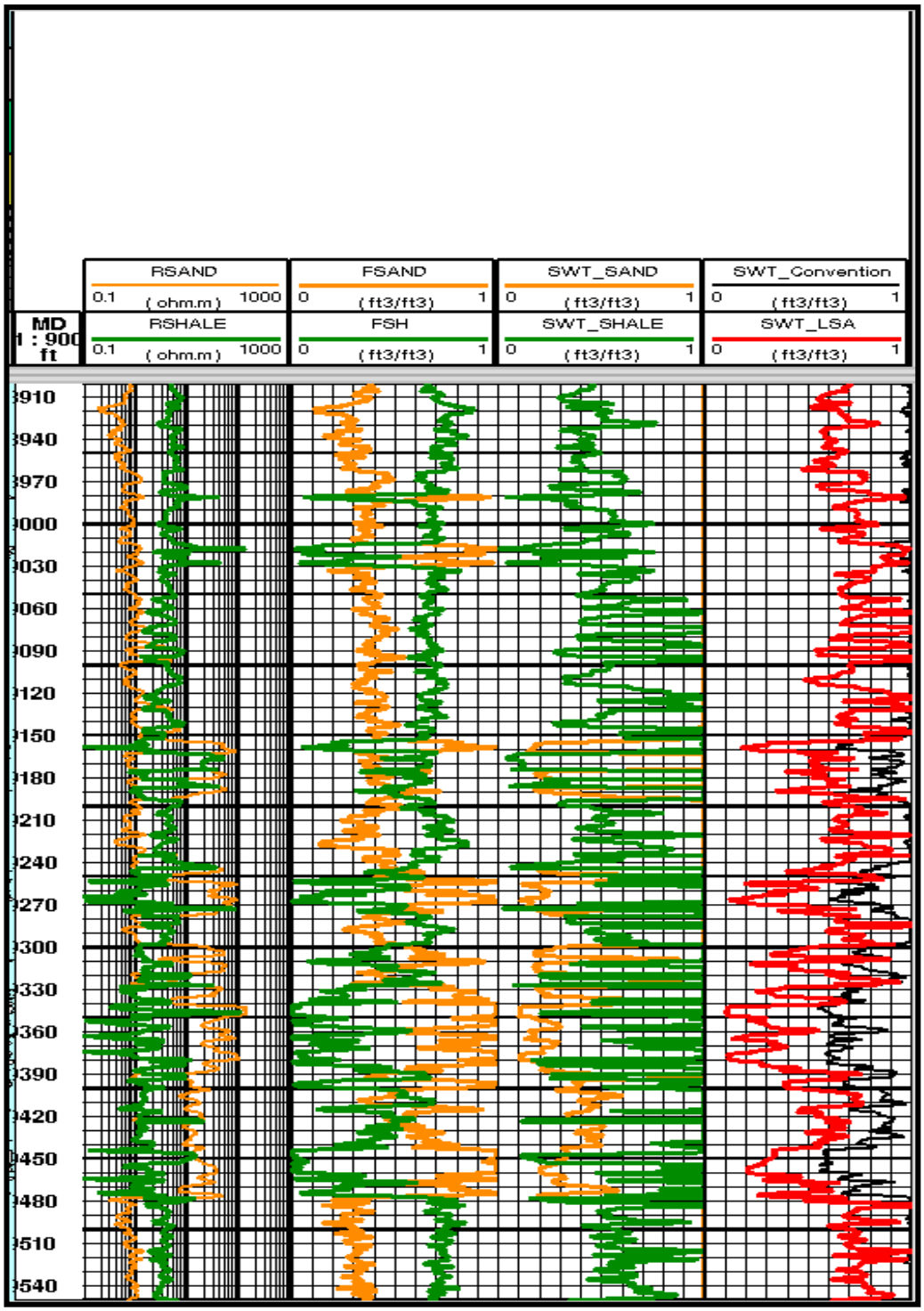

Figure 51. Depth Track. Track1: computed resistivity in the sand particles (RSAND) and in the shale particles (RSHALE). Track2: fraction volume of the sand (FSAND) and of the shale (FSH). Tack3: computed water saturation in the sand (SWT_SAND) and in the shale (SWT_SHALE). Track4: computed total water saturation from LSA Rv & RH using α=1 (SWT_LSA) and conventional total water saturation from only RH.

CHAPTER 6

Conclusion and Recommendations

This Thesis aimed to represent special techniques, called LSA, for evaluating thinly bedded low resistivity pays compared to the standard evaluations using only Gamma rays, Neutron-Density and horizontal resistivity in these thinly bedded low resistivity pays.

The LSA techniques that were involved in this Thesis included the Wireline NMR, borehole image logs and triaxial resistivity induction logs. The computed hydrocarbon volume from these LSA techniques was compared to the one from the standard evaluations.

The wireline NMR is capable of detecting low resistivity pays by separating free fluid from bound fluid volumes. A constrained log resolution enhancement processing utilizing the borehole image log (SRES curve) was performed to predict the actual log property of each bed (sand/shale) in the laminated sequence to compute a high resolution formation evaluation. The inverted vertical resistivity (Rv) and the horizontal resistivity (Rh) from the Triaxial resistivity induction logs improved the true sand formation resistivity (Rsand) and shale resistivity (Rshale) in order to compute the accurate water saturation in the laminations.

Two wells from fluvial and turbidite environments, exhibiting thinly bedded low resistivity in the pay zones, were discussed in this thesis.

The first well was a fluvio deltic sandstone formation that was evaluated by the conventional logs (Gamma rays, Neutron-Density and horizontal resistivity), Wireline NMR and the borehole image log. Combining the processed NMR together with the image logs gave high resolution formation evaluation compared to the standard evaluation in terms of clay volume (VCL), water saturation and therefore hydrocarbon saturations.

The second well was drilled in turbidite (deep water) environment. The Triaxial resistivity induction logs confirmed the increase in the hydrocarbon volume in the thinly bedded formation through the analysis of Rv and Rh. The analysis started by solving Clavaud equations simultaneously to invert sand beds resistivity (Rsand) , shale beds resistivity (Rshale) and the fraction volume of sand/shale beds. Then the water saturation in the sand beds and water saturation in the shale beds were computed using a resistivity-to- saturation transform e.g. Archie or Dual equations. After that, the volumetric average of the total volume of fluid in the laminated pay zone was computed and compared to the total volume of fluid in the same zone using only Rh in the analysis (standard evaluation).

All the interpretations in both case studies (Well A & Well B) were based on the knowledge of the studied area and adjacent wells exhibiting the same formations and depths. Additional data from tested core labs, downhole formation tester data and a drill stem tests are required to confirm the computed hydrocarbon volumes and producibility from these laminated sequences.

References

Akkurt,R., Ahmed, N.A., Behair,A. M., Rabaa, A.S., Crary,S.F., and Thum, S., 2008, NMR Radial Saturation Profiling For Delineating Oil-Water Contact in a High-Resisitivity Low-Contrast Formation Drilled With Oil-Based Mud,SPWLA 49th Annual Logging Symposium, 25-28 May 2008.

Akkurt, R., Bachman, H., Minh, C., Flaum, C., Carmona,R., Crary, S., Decoster, E., Heaton, N., et al., Nuclear Magnetic Resonance Comes Out of Its Shell, Oilfield Review Winter 2008/2009., 20, no.4.

Al-Fawwaz,A., Al-Maashrafi, N.,Butt, P., and Abdul Fareed, 2007, New Era of Formation Evaluation While Drilling of Complex Reservoirs in Saudi Arabia, SPE/IADC106596, Middle East Drilling Technology Conference & Exhibition 22-24 October 2007.

Al-Sabti, H.M., 1991, Lithology Determination of Clastic Reservoir Facies From Well Logs, Saudi Arabia, SPE21457, Middle East Oil Show held in Bahrain , 16-019Nov1991.

Asquith, G., and Krygowski, D., 2004, Basic Well Log Analysis, published by AAPG, Tusla, Oklahoma, second edition.

Bastia, R., Tyagi,A., Saxena, K., Klimentos, T., Altman,R., Alderman,S., and Bahuguna,S., 2007, Evaluation of Low-Resistivity-Pay Deepwater Turbidites Using Constrained Thin-Bed Petrophysical Analysis, SPE110752, Technical Conference and Exhibition held in Anaheim, California, 11-14 Nov 2007.

Chinese Science & Technology Paper Online, www.paper.edu.cn., Chapter3, Fundamentals of NMR Petrophysics.

Clavaud, J.B., Nelson, R., Guru, U.K., Wang, H.,2005,Field Example of Enhanced Hydrocarbon Estimation in Thinly Laminated Formation With A Triaxial Array Induction Tool: A laminated Sand-Shale Analysis With Anisotropic Shale, SPWLA 46TH Annual Logging Symposium, 26-29 June 2005.

Claverie, M., Aboel-Abbas, S., Mutiara, C.S., Harfoushian, H., Hansen, S., and Leech, R., 2006, Methods for Real-Time and High-Resolution Formation Evaluation and Formation Testing of Thinly Bedded Reservoirs in Exploration Wells, SPE101126, Asia Pacific Oil & Gas Conference and Exhibition held in Adelaide, Australia, 11-13 September 2006.

Claverie, M., Azam, H., Leech, R., and Dort, G. V.,2006, A Comparison of Laminated Sand Analysis Methods-Resistivity Anisotropy and Enhanced log rwesolution from Borehole Image, PGCE 2006.

Clavier, C., Coates, G., Dumanoir, J., 1977, The Theoretical and Experimental Bases for The Dual Warter Model For The Interpretation of Shaly Sands, SPE6859.

Cook, J., 1993, Use of Anisotropic Electrical Resistivity To Estimate The State of Compaction of Shale, unpublished results.

Daungkaew, S., Claverie, M., Cheong, B., Hansen, S., Leech, R., Azam, M.N..,Malim,E., Lasman, M.R., and Witjaksana R., 2008, Forecasting the Productivity of Thinly Laminated Sands with a Single Well Predictive Model, SPE116370, Asia Pacific Oil & Gas Conference and Exhibition held in Perth, Australia, 20-22 October 2008.

Devarajan, S., Toumelin, E., Torres-Verdin, C., and Thomas,E.C., 2006,Pore-Scale Analysis of The Waxman-Smits Shaly Sand Conductivity Model, SPWLA 47th Annual Logging Symposium, 4-7 June 2006.

Forsyth,D., Nawawi, H., and Ho, T.C., 1993, Review of Techniques for the Interpretation and Evaluation of Thin Sand Sequences, SPE25357, Asia Pacific Oil & Gas Conference and Exhibition held in Singapore, 8-10February 1993.

Guru, U., Heaton,N., Bachman, H.N., and LaVigne, J.,2005, Low-Resistivity Pay Evaluation Using Multidimensional and High-Resolution Magnetic Resonance Profiling, SPWLA 46th Annual Logging Symposium held in New Orleans, Louisiana, US, 26-29 Jun2 2005.

Hansen, S.M., and Fett,T., 1998, Identification and Evaluation of Turbidite and Other Deep Water Sands Using Open Hole Logs and Borehole Images, AAPG 1998 GCAGS/GCS

Hayden, R., Kostin, A, Jacobsen, S., Grant, J., Alderman,S., Katon,B., Liu, C.B., Schwartz, K., and Pham, T., 2009, Thin Bed Interpretation Techniques for Northwestern Gulf of Mexico Coastal and Offshore Clastics, SPWLA 50th Annual Logging Symposium, 21-24 June 2009.

Hook, P., Fairhurst, D., Rylander, E., Badry,R., Bachman,N., Crary, S., Chatawanich, K., and Taylor T., 2011, Improved Precision Magnetic Resonance Acquisition: Application to Shale Evaluation, SPE 146883, Annual Technical Conference and Exhibition held in Denver, Colorado, USA, 30 October-2 November 2011.

Joubert, J.B., 2009, Borehole Images Logs for Turbiditics Facies Identification, 71st EAGE Conference & Exhibition-Amsterdam, The Netherlands, 8-11 June 2009.

Joubert, J.B., and Maitan, V., 2010, Borehole Images Logs for Turbidite Facies Identification: Core Calibration and Outcrop Analogues, first break volume 28, June 2010.

Kantaatmadja, B.P., Hassan, A.M., Azam, M.N., Abdul Rahman, M.A.R., and Leech, R., 2010, Successful Application of Thin Bed Petrophysical Evaluation Workflow In Deep-Water Turbidite Environment: Case Studies From Fields Offshore Malaysia, PGCE 2010.

Kleinberg, R.L., Straley,C., Kenyon,W.E., Akkurt,R., and Farooqui, S.A., 1993,Nuclear Magnetic Resonance of Rocks: T1 vs. T2., SPE26470, 68TH Annual Technical

Conference and Exhibition of the Society of Petroleum Engineers held in Houston, Texas, 3-6 October 1993.

Kriegshauser, B.F., Fanini, O.N., Forgang, S., Mollison, R.A., Yu,L., Gupta, P.K., Koelman, J.M., and Popta, J.V., 2000, Increased Oil-In-Place In Low-Resistivity Reservoirs From Multicomponent Induction Log Data, SPWLA 41st Annual Logging Symposium , 4-7 June 2000.

Knighton, D., 1998, Fluvial Forms and Processes- A New Perspective: London, Arnold,383p.

Lawrence, D.A., 2002, Net Sand Analysis in Bedded Turbidite Reservoirs-Case Study Integrating Acoustic Images,Dipmeters and Core Data, SPWLA 43rd Annual Logging Sympsium, 2-5 June 2002.

Looyestijn, W.J., 2001, Distinguishing Fluid Properties and Producibility from NMR Logs, Nordic Energy Research Programme, Proceedings of the 6th Nordic Symposium on Petrophysics, Trondheim, Norwegian,15-16 May 2001.

Mcknight, T.L., and Hess, D., 2000, Physical geography-A landscape appreciation, 6th ed: Upper Saddle River, N.J., Prentic Hall, 604 p.

Minh, C.C., and Sundararaman, P., 2011, Nuclear-Magnetic-Resonance Petrophysics in Thin Sand/Shale,.SPE 102435, Annual Technical Conference and Exhibition, San Antonio, Texas,USA, 24-27 September 2006.

Minh, C.C, Clavaud, J.B., Sundararaman, P., Froment, S., Caroli, E., Billon, O., Davis, G., and Fairbairn, R., 2007, Graphical Analysis of Laminated Sand-Shale Formation in the Presence of Anisotropic Shales, SPWLA 48th Annual Logging Symposium, Austin, Texas, United States, 3-6 June 2007.

Mogbolu P.O., 2010, Identification and Quantification of Thinly Bedded Low Resistivity Pay in The Niger Delta, SPE 141133, Annual Technical Conference and Exhibition held in Florence, Italy, 19-22 September 2010.

Murray, D., Alderman, S., Fukuhara, M., and Namikawa, T., 2006, Vertical Resolution Enhancement of Geophysical Logs in Gas Hydrate Bearing Sands of the Nankai Trough, JPGU 2006, Chiba.

Newberry, B.M., Hansen, S.M., and Perrett, T.T., 2004, A Method for Analyzing Textural Changes Within Clastic Environments Utilizing Electrical Borehole Images, VOL 54, pages 531-540..

Pedersen, B.K., and Nordal,K., Petrophysical Evaluation of Thin beds: A Review of The Thomas-Stieber Approach, Course 24034 Formation Evaluation 1, Fall 1999, Norwegian University of Science and Technology.

Prasad,S.S., Sajith, C.S., and Bakshi,S.S., Evaluation of Low Resistivity Laminated Shaly Sand Reservoirs, 6th International Conference & Exposition on Petroleum Geophysics, Kolkata.

Schlumberger, 3rd Printing, May 1991, Schlumberger Educational Services.

Seifert, D., Crowell, A., Al-Dossary, S., and Crary, S., 2007, Thin-Bed Evaluation in Middle Eastern Sandstone Reservoirs, 1st Annual Middle East Regional SPWLA Symposium held in Abu Dhabi, UAE, 15-19 April 2007.

Shahid, M.A., Ur_Rahman,S., Syed, S. H., Zea-ul-Haq, M., Palekar,A.H., 2008, Identification of Low Resistivity Hydrocarbon Bearing Reservoirs in Lower & Middle Indus Basin Using Available Wireline Logs, SPE17497, Annual Technical Conference, Islambad 7-8 May 2008 .

Shanmugam, G., 1997, The Bouma Sequence and the Turbidite mind set, Earth-Science Reviews 4242 (1997) 201-229.

Slatt, R.M., 2001 Outcrop/Behind Outcrop Characterization of Deepwater (Turbidite) Petroleum Reservoir Analogs: Why and How, 2001-02 AAPG Distinguished Lecture.

Topical Conference on Low Resistivity Pay in Carbonates, Abu Dhabi 30th Jan.-2nd Feb. 2005. Abu Dhabi SPWLA Local Chapter.

Thomas, E.C., and Stieber, S.J., 1975, The Distribution of Shale in Sandstones and Its Effects Upon Porosity, SPWLA 16th Annual Logging Symposium, 4-7 June 1975.

Tyagi, A.K., Guha,R., Voleti,D., and Saxena, K., 2009, Challenges In The Reservoir Characterization of A Laminated Sand Shale Sequence, 2nd SPWLA-India Symposium, 19-20 November 2009.

Weber, R., Understanding Fluvial Systems: Wetlands, Streams, and Flood Plains, United States Department of Agriculture & Natural Resources Conservation Service, Issued February 2010.

Weimer,P., Slatt,R.M., Dromgoole,P., Bowman,M., and Leonard, A., Developing and Managing Turbidite Reservoirs: Case Histories and Experiences: Results of the 1998 EAGE/AAPG Research Conference.

Yadav,L., Dutta,T., Kundu, A., and Sinha, N., 2012, A New Approach For Construction Of High Resolution Earth model Using Dynamic Images For The Evaluation Of Very Thin Bed Reservoirs Of Krishna Godavari Basin East Coast, India, SPWLA 53rd Annual Logging Symposium, 16-20 June 2012.

Zhang,Z., Yuan,N., and Liu, R., Application of OpenMP to Wireline Triaxial Induction Logging in 1-D Layered Anisotropic Medium, Department of Electrical and Computer Engineering, University of Houston, 4800 Calhoun Rd, Houston, TX, 77204.

Vitae

Name	:Omar Abdullah Ba-Wazir
Nationality	:Yemeni
Date of Birth	:3/2/1984
Email	:bw_omar@yahoo.com
Address	:Al-Khobar 31952, P.O Box 2836
Academic Background	:Bachelor in Geophysics